The Company of **Biologists**

RESEARCH ARTICLE

Kinematics of sea star legged locomotion

Olaf Ellers, Melody Khoriaty and Amy S. Johnson*

ABSTRACT

Sea stars have slower crawling and faster bouncing gaits. Both speed and oscillation amplitude increase during the transition from crawling to oscillating. In the bouncy gait, oscillating vertical velocities precede oscillating horizontal velocities by 90 deg, as reflected by clockwise circular hodographs. Potential energy precedes horizontal kinetic energy by 9.6 deg and so they are nearly in phase. These phase relationships resemble terrestrial running gaits, except that podia are always on the ground. Kinetic and potential energy scale with body mass as $M_b^{1.1}$, with the change in kinetic energy consistently two orders of magnitude less, indicating that efficient exchange is not feasible. Frequency of the bouncy gait scales with $M_b^{-0.14}$, which is similar to continuously running vertebrates and indicates that gravitational forces are important. This scaling differs from the Hill model, in which scaling of muscle forces determine frequency. We propose a simple torque-stabilized inverted pendulum (TS-IP) model to conceptualize the dynamics of this gait. The TS-IP model incorporates mathematics equivalent to an angular spring, but implemented by a nearly constant upward force generated by the podia in each step. That upward force is just larger than the force required to sustain the underwater weight of the sea star. Even though the bouncy gait is the rapid gait for these sea stars, the pace of movement is still very slow. In fact, the observed Froude numbers (10^{-2} to 10^{-3}) are much lower than those typical of vertebrate locomotion and are as low or lower than those reported for slow-walking fruit flies, which are the lowest values for pedestrian Froude numbers of which we are aware.

KEY WORDS: Gait, *Asterias forbesi*, Biomechanics, Inverted pendulum, Froude number

INTRODUCTION

A gait is a pattern of motion characteristic of a range of speeds. Gaits typically change abruptly to a different gait at specific transition speeds (Alexander, 2003). The preferred or typical gait used at a certain speed uses less energy than alternative gaits that could be used at that speed (Hoyt and Taylor, 1981; Alexander, 1995; Minetti and Alexander, 1997; Saibene and Minetti, 2003; Snaterse et al., 2011; Andrada et al., 2020). Although gaits are rarely studied in underwater legged locomotors, there is a large literature on the kinematics of gaits in terrestrial legged locomotors and several well-established paradigms that are often used to frame kinematic, biomechanic and energetic arguments about terrestrial legged locomotion. While some terrestrial legged locomotors such as horses have several gait patterns such as walk, trot, canter and gallop

Department of Biology, Bowdoin College, Brunswick, Maine 04011, USA.

*Author for correspondence (ajohnson@bowdoin.edu)

O.E., 0000-0001-9161-5200; A.S.J., 0000-0003-2747-4786

(Nauwelaerts et al., 2015), terrestrial gaits have often been viewed through a dual kinematic characterization and contrast of walking versus running gaits.

In terms of models, an inverted pendulum model has been applied to walking gaits and a bouncing, spring-mass model has been applied to running gaits (reviewed in Dickinson et al., 2000), both of which are characterized by oscillations in the center of mass. More recently, the spring-loaded inverted pendulum (SLIP) model has been used to unify walking and running gaits under one model in contrast to the inverted pendulum model, which can only be applied to walking (Andrada et al., 2020). The need to incorporate hydrodynamics into spring-mass models for underwater legged locomotion was identified by Martinez et al. (1998), which motivated the modification of the SLIP model for crabs locomoting underwater (underwater spring-loaded inverted pendulum: USLIP) (Calisti and Laschi, 2017; Chellapurath et al., 2020).

In terms of speeds, among terrestrial legged locomotors, walking is a slower gait and running is a faster gait. Although it is quite possible to run slowly or to walk quickly, the fastest speeds cannot be achieved with a walking gait. The difference in speed between gaits can be considerable. For example, compared with walking, long distance runners approximately double their speed and sprinters approximately quadruple their speed. Speeds associated with novel gaits have also been considered in underwater legged locomotors. Some octopi accelerate into a bipedal gait (Huffard et al., 2005), and a fast underwater punting gait has been identified in crabs (Martinez et al., 1998), hippopotami (Coughlin and Fish, 2009) and crocodiles (Farlow et al., 2018). Brittle stars move rapidly by using their flexible arms to locomote using rowing and reverse rowing among other gaits (Arshavskii et al., 1976; Astley, 2012).

We focus here on sea stars, whose mode of locomotion has broadly been described as a crawl (Jennings, 1907; Cole, 1913; Brusca and Brusca, 2003; Montgomery and Palmer, 2012; Montgomery, 2014). In addition to the crawling gait, a second, faster oscillatory gait has been recently identified in the sea star *Protoreaster nodosus* (Ellers et al., 2014) and subsequently in *Asterias forbesi* and *Luidia clathrata* (Ellers et al., 2018; Johnson et al., 2019). We have also observed this bouncy gait in *Asterias rubens*, *Asterias amurensis*, *Pisaster giganteus* and *Acanthaster planci*. Sea stars locomote using numerous pressurized cylindrical tube feet, or podia, and the way in which those podia are used changes from the crawling to the bouncy gait. Heydari et al. (2020) created a model of podial function that has coordination among podia as an emergent property as speed increases from the crawling to the bouncing gait. Because different gaits can be used at some overlapping speeds, speed alone cannot be used to distinguish between gaits; it has to be considered in conjunction with other variables. In general, gaits can be considered as specific kinematic patterns and, in this paper, we describe several kinematic parameters for the sea star's gaits.

One kinematic feature of gaits is the frequency of the repeated motion. For terrestrial locomotors ranging in size from mice to horses, stride frequency f scales with mass M_b as $f \propto M_b^{-0.14}$ (Heglund et al., 1974), which is consistent with the hypothesis that

List of symbols and abbreviations

A	total cross-sectional area of all actively lifting podia
a_z	vertical acceleration
$(a_z)_{j,s}$	observed vertical acceleration, sth sea star, jth run
DFT	discrete Fourier transform
E_p	potential energy
$\bar{E}_p$	mean potential energy
ΔE_p	change in potential energy
$E_{p,amp}$	potential energy amplitude
E_{kh}	horizontal kinetic energy
$\bar{E}_{kh}$	mean horizontal kinetic energy
ΔE_{kh}	change in horizontal kinetic energy
$E_{kh,amp}$	horizontal kinetic energy amplitude
E_{kz}	vertical kinetic energy
$E_{k,total}$	total kinetic energy
$\Delta E_{k,total}$	change in total kinetic energy
$E_{k,amp,total}$	total kinetic energy amplitude
f	frequency
F_{xy_a}	horizontal force due to experimental observed a_{xy}
$(\bar{F}_{xy_a})_s$	mean rms(F_{xy_a}) for a sea star s
F_{z_a}	vertical force due to experimental observed a_z
$(\bar{F}_{z_a})_s$	mean rms(F_{z_a}) for a sea star s
F_z	resultant vertical force ($F_{z_p} - F_{z_{gb}}$)
$F_{z_{gb}}$	underwater vertical force (gravity minus bouyancy)
$(\bar{F}_{z_{gb}})_s$	mean underwater vertical force for a sea star s
F_{z_p}	upward podial forces
F_t	force tangent to the arc of a pendulum
Fr	Froude number
Fr_z	underwater Fr, using vertical accelerations
Fr_{xy}	underwater Fr, using horizontal accelerations
g	acceleration due to gravity
g_e	effective gravity
J	number of runs
l	length
M_b	body mass of animal
M_{PB}	mass of pendulum bob
M_f	mass of displaced fluid
$(M_b)_s$	mass of the sth sea star
ΔM	sea star mass minus mass of displaced water
P	podial hydrostatic pressure
ΔP	difference in pressure across the ampullar wall
R	radius of curvature of the ampullar wall
ΔR	ampullar wall thickness
rms	root mean square
s	sea star number
S	total number of sea stars
SLIP	spring-loaded inverted pendulum model
TS-IP	torque stabilized inverted pendulum model
t	time
U	speed
USLIP	underwater spring-loaded inverted pendulum model
v_x, v_y	velocity in the x and y directions, from bottom videos
$v_{z,side}$	velocity in the z direction, from side videos
$v_{x,side}$	velocity in the x direction, from side videos
v_{xy}	speed in the horizontal plane
v_{xyz}	magnitude of the 3D velocity vector
x, y, z	axes in the right-handed coordinate system
X	independent variable
Y	dependent variable
$\bar{z}$	mean z displacement over an entire video
Δz	vertical location relative to a reference height
θ	angle of pendulum rod to vertical
κ	coefficient of added mass
λ	step length
ρ	sea star density
ρ_{PB}	pendulum bob density
ρ_f	fluid density
σ	podial muscle stress
τ	period in air
τ_u	period of an underwater pendulum
υ	sea star volume
ϕ_j	phase shifts for each of j runs for a given sea star
$\bar{\phi}$	phase shift mean for all the runs of a given sea star
ω	angular frequency

gait frequency is controlled by the physical dimensions of a pendulum driving the oscillatory motion, as described by Alexander and Jayes (1983). In that hypothesis, gravitational forces are important in driving the motion, and the kinematics and dynamics can be described using the Froude number, which is the ratio of inertial to gravitational forces; gait transitions occur at specific Froude numbers. In contrast, oscillatory frequency of the limbs of a wide range of swimming seabirds, cetaceans and pinnipeds scaled with mass as $f \propto M_b^{-0.29}$ (Sato et al., 2007, 2010), supporting the hypothesis first suggested by Hill (1950), whereby muscle characteristics explain this scaling relationship.

In addition, phase relationships in energy and velocities are frequently used to characterize gaits. The phase relationship of kinetic energy and potential energy determines the potential for exchange between these two energies and is one way of distinguishing between walking and running gaits. In a perfect pendulum, the change in kinetic energy and potential energy are exactly out of phase and of equal magnitude such that all the energy can be perfectly recovered in each swing, with no energy loss. Similarly to a pendulum, kinetic energy and potential energy fluctuate out of phase and are of similar magnitude during the terrestrial walking gait; however, the kinetic energy–potential energy phase relationship and energy recovery is imperfect. In human walking, for example, Cavagna and Legramandi (2020) found a maximum energy recovery of 66%. Among the highest energy recoveries reported are, surprisingly, for waddling penguins (80%); Griffin and Kram (2000) found that the penguin's waddling gait achieved this remarkable efficiency by causing the kinetic energy and potential energy to fluctuate more completely out of phase and to be of more similar magnitude. In contrast, in stealthy walking in cats, low energy recovery between kinetic energy and potential energy was a consequence of a less efficient phase relationship between these two energies (Bishop et al., 2008). In running, these energies fluctuate in phase; for example, Cavagna et al. (1964) reported a phase shift between kinetic and potential energy of, at most, about 10 deg. The phase relationship between vertical and horizontal velocities, shown on plots called hodographs, can also be used to characterize gaits. In particular, counter-clockwise hodographs are characteristic of walking, whereas clockwise hodographs are characteristic of running (Usherwood, 2010). Experimental hodographs have not previously been examined for underwater legged animal locomoters, although Calisti and Laschi (2017) have produced theoretical limit cycles, based on the USLIP model, whose projections are hodographs.

In this paper, we kinematically characterize the crawling and oscillatory gaits of the sea star *Asterias forbesi*. Some kinematic variables we consider are: speed, frequency, kinetic and potential energy changes, phases between vertical and horizontal velocities (i.e. hodographs), and phases between kinetic and potential energy. We measure changes with mass of the kinematic variables: frequency, speed, vertical position, and kinetic and potential energy. We further measure changes with mass of the morphological variables: density, underwater weight and podial leg length. To obtain these kinematics, we tracked synchronized side and bottom videos of 54 individuals of the sea star *A. forbesi*, ranging in mass over three orders of magnitude.

We calculated Froude numbers associated with the sea star oscillatory gait and we evaluate whether gravitational forces, as in Alexander and Jayes (1983) or muscle forces, as in Hill (1950), drive the scaling of frequency with mass. Finally, we developed a version of a simple inverted pendulum model that is consistent with the observed kinematics of the sea star oscillatory gait and provides some insight into the dynamics of the gaits.

MATERIALS AND METHODS

Animal collection and maintenance

Adult *Asterias forbesi* (Desor 1848) were hand-collected in rocky intertidal and shallow subtidal areas adjacent to Basin Point, Harpswell, ME (43.74°N, −70.04°W) and the Rockland Breakwater, Rockland, ME (44.11°N, −69.08°W). Sea stars were maintained in recirculating seawater aquaria at 12–13°C and 30–33 ppt salinity and were fed weekly with mussels and barnacles. Sea stars were acclimated in these aquaria for at least 2 weeks prior to locomotion trials.

Locomotion trials

A subset of 54 sea stars were individually filmed in runways with recirculating sea water maintained at 12–13°C and 30–33 ppt. Sea stars were filmed over 6 weeks during the summer of 2015 and 7 weeks during the summer of 2017.

Two runways were used, with cross sections: (1) 15 cm wide by 10 cm deep and (2) 36 cm wide by 15 cm deep. Locomoting sea stars were filmed at 30 fps (resolution 1920×1080 pixels) with two Nikon 5200 SLR cameras equipped with SanDisk Extreme Pro95 MB s^{-1} SDXC I V90 C10 U3 memory cards. The lines of sight of the cameras were normal to the bottom and side of the runway, and the lines of sight intersected with the side camera line of sight being 1 cm above the bottom surface and the bottom camera line of sight being centrally located in the bottom of the tank. The bottom camera was equipped with a Nikon DX AF-S Nikkor 10–24 mm 1:3.5–4.5G ED lens, the side camera was equipped with a Nikon DX AF-S Nikkor 18–55 mm 1:3.5–5.6G VR lens. Cameras were synchronized using wireless WR-T10 and WR-R10 controllers.

Camera synchronization was checked by filming the sudden blocking of a laser light beam by a falling object. This blockage resulted in the disappearance of a laser spot in both the side and bottom videos; the difference (side–bottom) of the frame number in which the disappearance of that light spot was detected in the two views was determined; difference in total frames in the video of each view was also calculated. The average difference in frame in which the laser spot disappeared was −0.67±2.5 (mean±s.d.) frames and the average difference in total frames was −0.66±2.2 frames (n=100 side and bottom pairs). In addition, we checked the synchronization of the cameras during the filming of the sea stars by comparing the total frames in paired side and bottom videos for all videos used in this study; the average difference in total frames for these video pairs was −0.14±1.9 frames (n=128 side and bottom pairs).

As a final synchrony check on the sea star videos, we used unfiltered *x*-position data from the side videos and unfiltered *x*-position data from the bottom videos to calculate *x*-velocity from the two views (see Fig. 1 for the coordinate system). We used cross-correlation between those two *x*-velocities to determine phase shifts between the *x*-position as seen from the side camera and the *x*-position as seen from the bottom camera. Mean phase shift among all films (n=128) was 0.021±0.059 radians (1.2±3.4 deg; mean±s.d.), with the side videos preceding the bottom videos on average by that amount. A sign test (P<0.001) shows that side camera tended to start
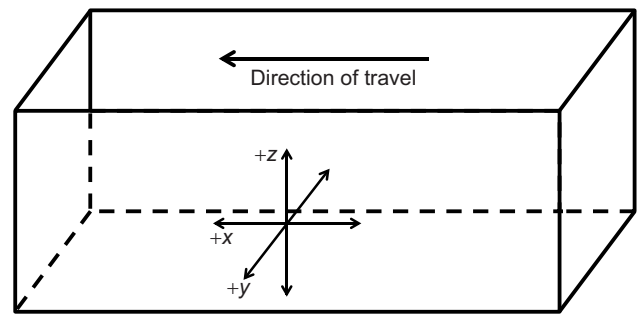

Fig. 1. The coordinate system is right handed, and oriented with the positive *x*-axis in the direction of travel.

before the bottom camera to a statistically detectable extent. On average, this imposes a 1 deg phase shift and limits the ability to detect phase shifts in kinematic variables to phase shifts greater than 1 deg.

We ensured movement from right to left from the point of view of the cameras in the following way. The movement was encouraged by gentle poking with a blunt rod or by inverting the sea stars and allowing them to right themselves. Sea stars can move with any arm or interarm leading and the leading region can change continuously or spontaneously. For a given run, and before starting to film, we noted the leading region of the sea star and gently rotated the moving sea star so that the leading region was oriented toward the left end of the runway from the point of view of the cameras. At the end of each run, two square layout miters (Shinwa, Japan) were placed in the tank to scale the videos.

Kinematic variables

The right-handed coordinate system we used is shown in Fig. 1. Only portions of runs in which the sea stars moved in the positive *x*-direction without touching the walls of the tank were analyzed.

Sea star movement was tracked using Tracker Video Analysis and Modeling Tool 5.1 (https://physlets.org/tracker/). The mouth and the highest point on the top of the sea star were used as tracking points for the bottom and side videos, respectively.

A total of 128 matched bottom and side videos of 54 sea stars were analyzed (1–6 videos per sea star); the average duration of videos was 39±18 s (mean±s.d.; range: 10–107 s).

Time and position data from Tracker were smoothed using 30-point moving averages as a low-pass filter. The moving average was applied to the time array and to the position array (see supplementary Materials and Methods section 1 for further details). Such averaging results in arrays that are shorter than the originals by 29 points, with equal amounts of information being lost from both ends of the arrays. The time interval between points is nevertheless maintained and is equal to the sampling interval, i.e., the frame interval of the video recording. The smoothed time-array was then renumbered starting at zero.

This moving average filter preserves the motion at the main underlying frequency of the bouncy gait and rejects high frequency noise while maintaining much, or most, of the amplitude of the major low frequency motions of the sea stars (see supplementary Materials and Methods section 2 for further details; Figs S1–S5).

The moving average filter does not introduce any phase distortion into the signal. Therefore, it is possible to calculate phase shifts from the filtered data. Nevertheless, because some kinds of filters do introduce phase distortion, we used unfiltered data and cross-correlation analysis to determine the phase shifts between the

horizontal speed and the vertical velocity and between the kinetic and potential energy.

Calculating velocities and accelerations, indeed calculating any higher derivatives from raw data, has the effect of increasing the importance of higher frequencies in the signal (see supplementary Materials and Methods section 3 for further details; Eqns S1–S3, Figs S2D, S4, S5). This problem becomes more severe the higher the derivatives. For this reason, when calculating accelerations, we used a slightly less aggressive (not moving average) low pass filter with a 1 Hz cut off on the position data, implemented in Mathematica (Wolfram) before calculating the accelerations as a function of time for each video.

Finally, velocity squared data, such as kinetic energy, also increases the importance of higher frequencies (see supplementary Materials and Methods section 4 for further details; Eqns S4–S7). Therefore, as a sensitivity analysis, we present in the supplementary Materials and Methods, an alternative fitted scaling equation of the kinetic and potential energy that is produced with 1 Hz low pass filtered position data.

With the exception of acceleration and phase calculations, calculations were done on the smoothed, renumbered time and position signal. In particular, smoothed time and position data were used to calculate position changes and velocity components (v_x, v_y, v_z). Horizontal speed v_{xy} was calculated at each time from the velocity components v_x and v_y. Vertical velocity v_z was calculated from the side videos and v_x and v_y were calculated from the bottom videos. For purposes of perspective error analysis, $v_{x,\text{side}}$ was also calculated from the side videos.

Vertical displacement Δz was calculated as:

$$\Delta z = z - \bar{z}, \tag{1}$$

and $\bar{z}$ is the mean over an entire video. As a variable to examine scaling of vertical displacement relative to mass, we also calculated rms(Δz), where rms is the root mean square (RMS). The RMS is a convenient measure of signal size especially when there are a few frequencies all contributing to the overall signal size (see supplementary Materials and Methods section 5 for further details; Eqns S8,S9). The range in Δz can be used as a proxy for podial leg length; for this purpose we calculated $2\sqrt{2}\,\text{rms}(\Delta z)$.

Assessment of perspective error in side videos
Fractional perspective error in the side videos was estimated as:

$$\left| \frac{v_x - v_{x,\text{side}}}{0.5(v_x + v_{x,\text{side}})} \right|. \tag{2}$$

Across 128 matched side and bottom videos and 54 sea stars, the mean fractional perspective error was 0.10±0.0035 (mean±s.e.m.). A plot of $v_{x,\text{side}}$ as a function of v_x is expected to have a slope of 1 in the absence of perspective error; the observed mean of the slopes is 1.02±0.0078 (R^2=0.94±0.0044).

Speed, frequency and gait
Frequency spectra of horizontal plane speed oscillations were estimated using the Fourier function in Mathematica, which performs a discrete Fourier transform (DFT). Frequency resolution equals frame rate divided by the number of frames in a video. Across the 128 video pairs the mean frequency resolution was 0.03 Hz, with a range from 0.1 to 0.01 Hz. We report amplitudes only from frequencies f where 0.1 Hz≤f≤1 Hz. Amplitudes from higher frequencies are negligibly small and amplitudes from lower frequencies represent longer term changes in

behavior such as changes in gait. The fundamental frequency was taken to be the frequency with the largest speed amplitude over the time interval analyzed, which was the whole length of each video except when moving windows were analyzed.

Such moving windows were used in determining the relationship between the mean v_{xy} in a time interval and the amplitude of the fundamental frequency for portions of a given video. This is useful for determining changes in the amplitude of the fundamental frequency as gait changes. For this purpose, DFTs and moving averages were performed on 5 s or 45 s windows starting every second. Such analyses from three characteristic videos are shown in the results.

Mass and density
Mass
Mass was obtained for 86 sea stars, including for the subset of 54 used in kinematic analyses. Mass was measured using an Ohaus Adventure digital precision balance Model AX423 (precision: ±0.001 g). Underwater weights were obtained by hanging each sea star from a force beam into a bucket of seawater using a Kyowa force transducer model LVS-20GA, a DPM-911B strain amplifier, micro 1401 Cambridge Electronic Design AtoD converter and Spike II version 7.14 data acquisition software (precision: ±0.001 g). Masses (three to five measurements per sea star) and underwater weights (one to five measurements per sea star) were determined.

A sea star of mass M_b displaces a fluid of mass M_f generating an underwater vertical force due to gravity and buoyancy $F_{z_{gb}}$:

$$F_{z_{gb}} = (M_b - M_f)\boldsymbol{g} = \Delta M_b\,\boldsymbol{g}, \tag{3}$$

where ΔM_b is the difference in sea star and displaced masses and g is the gravitational acceleration. The ΔM_b can be determined experimentally by dividing the underwater weight in Newtons by $\boldsymbol{g}$.

Density
The definition of density implies that:

$$\frac{\rho}{\rho_f} = \frac{M_b}{M_f}, \tag{4}$$

where ρ is sea star density and ρ_f is fluid density. For our experiment we used a sea water density of 1025 kg m^{-3}, which corresponds to seawater at 13°C and 33 ppt. Combining Eqn 3 and Eqn 4 gives an equation for calculating density from the measured M_b and ΔM_b:

$$\rho = \frac{M_b\,\rho_f}{M_b - \Delta M_b}. \tag{5}$$

Eqn 5 is equivalent to:

$$\frac{\Delta M_b}{M_b} = \left(1 - \frac{\rho_f}{\rho}\right), \tag{6}$$

which gives a ratio for expressing the fraction of mass not supported by buoyancy.

Eqn 6 is an alternative to using an effective gravity g_e (Martinez et al., 1998; Chellapurath et al., 2020) where, using Eqns 3 and 6:

$$\boldsymbol{g}_e = \frac{F_{z_{gb}}}{M_b} = \frac{\Delta M_b}{M_b}\boldsymbol{g} = \left(1 - \frac{\rho_f}{\rho}\right)\boldsymbol{g}. \tag{7}$$

We prefer using Eqn 6 because it makes explicit that $\boldsymbol{g}$ is a constant, whereas $\boldsymbol{g}_e$ depends on the assumption of constant density. It has been our experience that the density of benthic animals often scales with mass making the use of an effective gravity potentially misleading.

Energies

Data from the side videos were used to calculate the change in potential energy ΔE_p and data from the bottom videos were used to calculated the change in kinetic energy associated with the component of velocity in the horizontal plane ΔE_kh relative to respective mean energies in each video.

The change in potential energy was calculated as:

$$\Delta E_\mathrm{p} = (E_\mathrm{p} - \bar{E}_\mathrm{p}), \tag{8}$$

where the potential energy E_p is:

$$E_\mathrm{p} = \Delta M_\mathrm{b} \boldsymbol{g} \Delta z. \tag{9}$$

Change in horizontal kinetic energy was calculated as:

$$\Delta E_\mathrm{kh} = (E_\mathrm{kh} - \bar{E}_\mathrm{kh}), \tag{10}$$

where:

$$E_\mathrm{kh} = \frac{1}{2} M_\mathrm{b} v_{xy}^2. \tag{11}$$

To compare temporal patterns of these energies, they were plotted as functions of time for three characteristic videos in the results. In addition, potential energy amplitude $E_\mathrm{p,amp}$ and the kinetic energy amplitude $E_\mathrm{kh,amp}$ for each video were calculated as:

$$E_\mathrm{p,amp} = \sqrt{2}\,\mathrm{rms}(\Delta E_\mathrm{p}), \tag{12}$$

and

$$E_\mathrm{kh,amp} = \sqrt{2}\,\mathrm{rms}(\Delta E_\mathrm{kh}). \tag{13}$$

The mean values of $E_\mathrm{p,amp}$ and $E_\mathrm{kh,amp}$ for each sea star were obtained by averaging values for all videos of a given sea star. These quantities are of interest because they allow the comparison of the amount of energy that could potentially be exchanged between potential and kinetic energy.

To assess the degree to which total energy amplitude $E_\mathrm{k,amp,total}$ reflects $E_\mathrm{kh,amp}$, we calculated the ratio $\frac{E_\mathrm{kh,amp}}{E_\mathrm{k,amp,total}}$, where $E_\mathrm{k,amp,total}$ was calculated in a manner analogous to $E_\mathrm{kh,amp}$, where total kinetic energy $E_\mathrm{k,total}$ is:

$$E_\mathrm{k,total} = \frac{1}{2} M_\mathrm{b} v_{xyz}^2, \tag{14}$$

and v_{xyz} is the magnitude of the 3D velocity vector.

Scaling

Allometric relationships were analyzed using double logarithmic plots for the following dependent variables: sea star density, fundamental frequency, mean horizontal speed, ΔM_b, $\mathrm{rms}(\Delta z)$, $E_\mathrm{p,amp}$ and $E_\mathrm{kh,amp}$. To do this, both the dependent variable and the independent variable (M_b) were log-transformed and linear regression on the log–log transformed data was performed to evaluate the exponential trends observed. Plots of only the first three and last two variables are shown in the results. The density was calculated from the mean M_b and ΔM_b using Eqn 5 for each sea star. The frequency was the mean over all videos of each sea star of the fundamental frequencies measured in each video. The speed, rms (Δz), $E_\mathrm{p,amp}$ and $E_\mathrm{kh,amp}$ were the means over all videos of each sea star in each video. Exponentiating both sides of the equation for the linear relationship between the log-transformed variables gives the coefficient and exponent of the exponential relationship.

In addition, a paired t-test on log-transformed energies was used to test the null hypothesis that $E_\mathrm{p,amp}$ and $E_\mathrm{kh,amp}$ were equal in a given sea star. Finally, because theory developed in the discussion predicts a scaling exponent of 1.3 for energy amplitudes, we tested the null hypothesis that the slopes of the log-log regressions did not differ from a slope of 1.3 using an extra sum-of-squares F-test in Prism (GraphPad).

Hodographs and phase shifts

Hodographs plotting v_z against v_{xy} were produced to observe phase shifts and to compare patterns between crawling and oscillating gaits. In addition, hodograph-like plots were made of ΔE_p against ΔE_kh to describe the temporal pattern of change in energies. Characteristic patterns from three videos are presented in the results.

For all 128 videos, we estimated the phase shifts on the unfiltered data between ΔE_kh and ΔE_p, and between v_{xy} and v_z by using a cross-correlation analysis written in Mathematica (by O.E.). Means for each sea star were determined using polar statistics. Angular mean was calculated as:

$$\bar{\phi} = \mathrm{atan2}\left(\frac{1}{J}\sum_{j=1}^{J}\sin\phi_j, \frac{1}{J}\sum_{j=1}^{J}\cos\phi_j\right), \tag{15}$$

where $\bar{\phi}$ is the phase shift mean for all the runs of a given sea star, and ϕ_j are the phase shifts for each of J runs for each of the energy and velocity pairs for a given sea star. An angle mean similar to Eqn 15 was also used to calculate the mean phase shift for all sea stars from the individual means of each sea star. Depending on underlying distributions in the data either t-tests or non-parametric sign-tests or Mann–Whitney U-tests were used to compare phase shift between vertical and horizontal velocities and between potential and kinetic energy with values of $\pi/2$ and zero, respectively and the mean phase shift between energies compared with that between cameras.

Gravitational versus accelerative forces

The mean underwater vertical force due to gravity and bouyancy acting on a specific sea star $(\bar{F}_{z_\mathrm{gb}})_s$ was calculated from Eqn 3 as:

$$(\bar{F}_{z_\mathrm{gb}})_s = (\Delta \bar{M}_\mathrm{b})_s\,\boldsymbol{g}, \tag{16}$$

where $(\Delta \bar{M}_\mathrm{b})_s$ is the average ΔM_b for the sth sea star.

The underwater vertical and horizontal forces due to accelerations acting on a specific sea star were determined as follows. Vertical velocities v_z and horizontal speeds v_{xy}, were calculated from 1 Hz low pass filtered position data and were then used to calculate vertical accelerations a_z and horizontal accelerations a_{xy}.

The mean of the observed experimental $\mathrm{rms}(a_z)$ for a specific sea star was estimated over several runs as:

$$(\bar{a}_z)_s = \frac{1}{J}\sum_{j=1}^{J}\mathrm{rms}(a_z)_{j,s}, \tag{17}$$

where $(a_z)_{j,s}$ is the observed vertical acceleration as a function of time for the sth sea star and the jth run.

The mean rms of forces $(\bar{F}_{z_a})_s$ associated with the observed experimental vertical accelerations acting on a specific sea star averaged over several runs were estimated as:

$$(\bar{F}_{z_a})_s = (\bar{M}_\mathrm{b})_s\,(\bar{a}_z)_s, \tag{18}$$

where $(\bar{M}_\mathrm{b})_s$ is the mean mass for the sth sea star. The mean rms of forces associated with the observed experimental horizontal accelerations acting on a specific sea star $(\bar{F}_{xy_a})_s$ were estimated in the appropriate analogous way.

These accelerative forces are compared with gravitational minus bouyancy forces over all sea stars by calculating two kinds of

underwater Froude numbers Fr relative to vertical and horizontal accelerations:

$$Fr_z = \frac{1}{S} \sum_{s=1}^{S} \frac{(\bar{F}_{z_a})_s}{(\bar{F}_{z_{gb}})_s}, \qquad (19)$$

and

$$Fr_{xy} = \frac{1}{S} \sum_{s=1}^{S} \frac{(\bar{F}_{xy_a})_s}{(\bar{F}_{z_{gb}})_s}, \qquad (20)$$

where S is the total number of sea stars in the kinematic analysis.

As a sensitivity analysis on the effects of filtering, in addition to calculating the Froude numbers from 1 Hz low pass filtered position data, we also calculated them from data low pass filtered with 2, 3 and 4 Hz cut offs (see supplementary Materials and Methods section 6 for further details; Table S1).

Analysis software
Data were processed using Mathematica (v. 12.0.0.0) and Julia (v. 1.5). Figures were created using Prism (v. 7.0a) and Julia packages: GRUtils (https://juliapackages.com/p/grutils), CSV (https://juliapackages.com/p/csv) and DataFrames (https://juliapackages.com/p/dataframes). Statistical analyses were done using Prism, Mathematica and SPSS Statistics (v. 26.0.0.0). Mathematica and Julia codes were custom written in house.

RESULTS
Kinematic variables
Sea stars exhibit consistent patterns of motion (Fig. 2). They have two gaits: a slower crawling gait and a faster oscillatory gait in which the sea star oscillates vertically. During the oscillatory gait the vertical displacements and speeds oscillate and the horizontal speeds oscillate around an average speed. Whereas the average vertical speed is close to zero, the average horizontal speed is several mm s^{-1} and the minimum horizontal speed during a video is typically greater than zero. While transitioning to an oscillatory gait the sea star vertical height increases and develops vertical oscillations that tend to become more regular.

Speed, frequency and gait
As sea stars transitioned from the crawling to the oscillatory gait, the vertical oscillations increased and the horizontal and vertical speed oscillations increased in amplitude (Figs 2,3). Each sea star has a characteristic frequency that can be determined by doing DFTs over the period of a video; we report those for the v_{xy} oscillations. The frequencies we observed for these sea stars were between 0.14 and 0.40 Hz corresponding to periods between 7.2 and 2.5 s. While the highest period-averaged horizontal speeds are achieved during the oscillatory gait, most of the increase in period-averaged horizontal speed occurs during the crawling gait. There are more gradual increases in period-averaged horizontal speed with increasing oscillation amplitude of the horizontal speed during the oscillatory gait.

Scaling of density, frequency, speed and vertical displacement
Sea star density was a function of mass (log–log regression: $F_{1,84}=37$, $P<0.0001$; Fig. 4A) with heavier sea stars having a lower density. During the oscillatory gait, mass of the sea stars accounted for 53% of the variation in the fundamental frequency of horizontal speed oscillations with heavier sea stars oscillating at
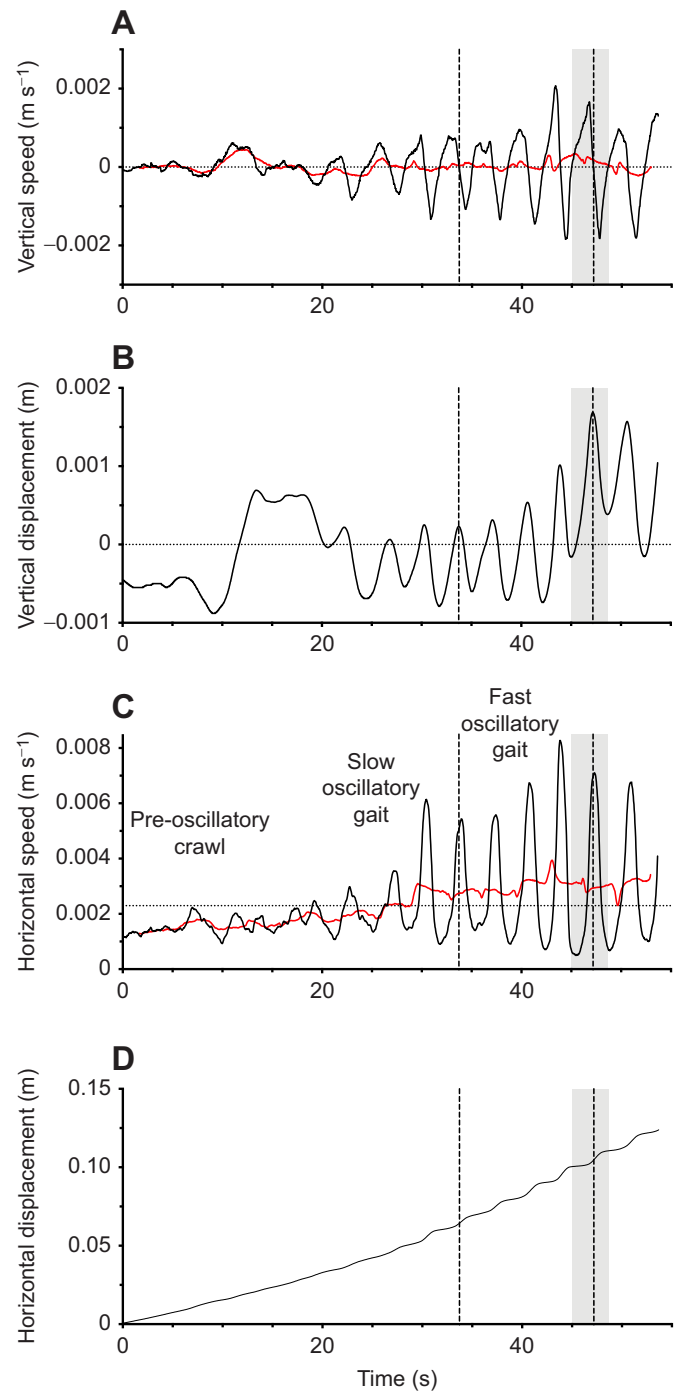

Fig. 2. The transition from crawling to oscillatory gait in a 24 g sea star (*Asterias forbesi*). (A) Vertical velocity (v_z), shown as a 1 s moving average (black line) and a 3.36 s moving average based on the fundamental period for these data (red line). (B) Vertical displacement (Δz) of the sea star, shown as a 1 s moving average, with the mean vertical displacement indicated by the dotted zero line. (C) Speed in the horizontal plane (v_{xy}), shown as a 1 s moving average (black line) and a 3.36 s moving average (red line), with the mean v_{xy} indicated by the horizontal dotted line. (D) Horizontal displacement shown as a 1 s moving average. The two vertical dashed lines are placed at the times of two peaks in vertical displacement and show that peak horizontal speeds are nearly in phase with peak vertical displacements of the sea star. These data illustrate a typical pattern, where sea stars crawl with increasing Δz and v_{xy}, transitioning to low amplitude and then high amplitude Δz oscillations. The area shaded in grey indicates the cycle that is plotted in Fig. 7A.
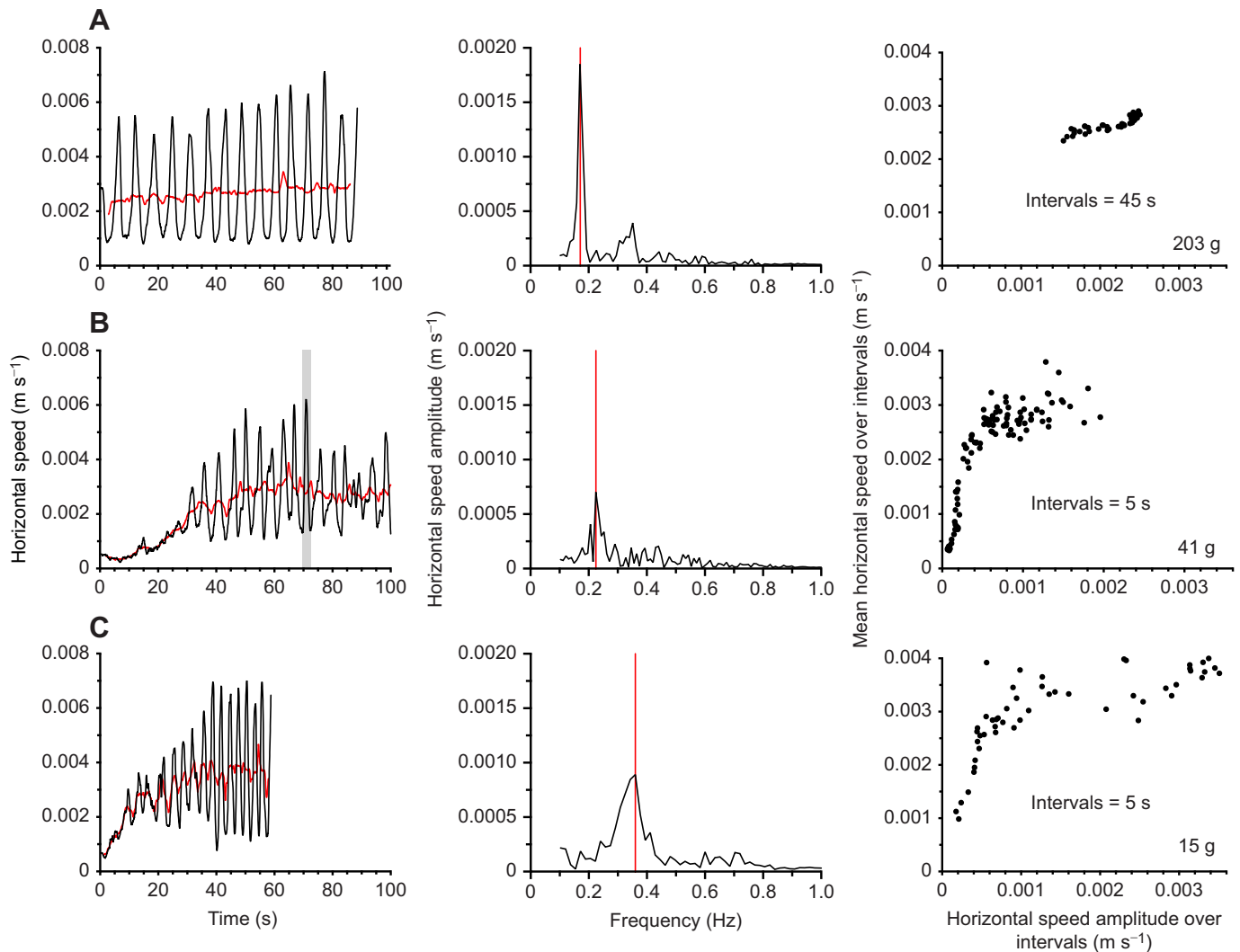
Fig. 3. Examples from videos of three locomoting sea stars. (A–C) v_{xy} as a function of time (left), shown as a 1 s moving average (black line) and longer moving averages based on the fundamental periods determined for each video (red lines; A, 5.9 s; B, 4.4 s; C, 2.8 s) for sea stars of mass 203 g (A), 41 g (B) and 15 g (C). The area shaded in grey indicates the cycle that is plotted in Fig. 7B. DFTs with the v_{xy} oscillation amplitude as a function of frequency (middle), where the vertical red line indicates the fundamental frequency f, which has the largest v_{xy} amplitude. Mean v_{xy} over intervals shown as a function of v_{xy} amplitude over intervals (right); means were calculated for the indicated intervals starting each second. Most of the increase in v_{xy} occurred during low amplitude oscillations of less than 4×10^{-4} m s^{-1} (i.e. during crawling); further increases in speed with increasing v_{xy} amplitudes were more gradual.

lower frequencies (log–log regression: $F_{1,52}=58$, $P<0.0001$; Figs 3, 4B, 5). Mass accounted for 14% of the variation in mean speed, with heavier sea stars moving faster (log–log regression: $F_{1,52}=8.8$, $P=0.005$; Fig. 4C).

Horizontal and vertical oscillations in speed were mechanically linked since for 84% of the videos the fundamental frequency was identical when calculated from horizontal versus vertical velocities. In the 16% of cases where they were not identical, they were similar; the mean absolute value of the difference was 0.04 Hz, which was below our ability to resolve differences given the mean frequency resolution of 0.03 Hz.

Eqn 6 indicates that ΔM_b is a linear function of M_b if sea star density ρ is constant, but a log–log regression gives:

$$\Delta M_b = 0.11 M_b^{0.95 \pm 0.016 \text{ s.e.m.}}, \tag{21}$$

with an $R^2=0.98$ (log–log regression: $F_{1,52}=3500$, $P<0.0001$), indicating that sea star density changes slightly but systematically with sea star mass, which is also supported by Fig. 4A. Eqn 21 gives

a useful approximate rule that $\Delta M_b/M_b \approx 0.1$. However, for the sea stars in Fig. 4A, the range of density from ≈ 1100–1200 kg m^{-3} encompasses a range of g_e/g (Eqn 7) from 0.054 to 0.14, a difference of a factor more than two. Thus, the force that sea stars need to exert to support their weight underwater is about 10% of what it would be on land, but for more precise calculations or scaling considerations it may be necessary to consider that systematic trend with mass.

Vertical displacement was also a function of sea star mass:

$$\text{rms}(\Delta z) = 2.8 \times 10^{-4} M_b^{0.15 \pm 0.03 \text{ s.e.m.}}, \tag{22}$$

where units of mass are in g and units of vertical displacement are in m, and with an $R^2=0.32$ (log–log regression: $F_{1,52}=25$, $P<0.0001$) indicating that heavier sea stars have slightly greater, but highly variable, changes in oscillatory height.
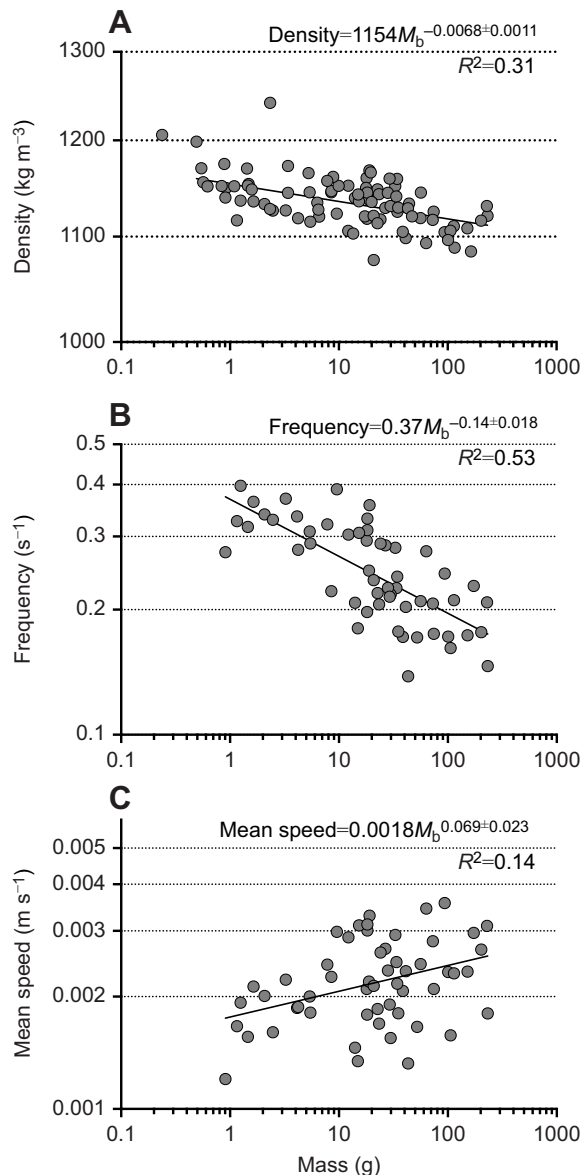
Fig. 4. Logarithmic plots of sea star density, fundamental frequency of the oscillatory gait and mean horizontal speed. (A) Sea star density, (B) fundamental frequency of the oscillatory gait, and (C) mean horizontal speed as a function of sea star mass. Density and fundamental frequency decreased and mean horizontal speed increased with increasing mass of sea stars. Data points represent the mean values for each sea star. Units in the fitted equations are as on the axes in the figures. In (A) two of the plotted points were excluded from the regression analysis based on Cook's distance. Errors shown are s.e.m.

Fig. 5. Change in kinetic energy and potential energy during the oscillatory gait in three individual sea stars. (A–C) Change in KE (ΔE_{kh}, left axes, dashed lines, Eqn 10) and PE (ΔE_p, right axes, solid lines, Eqn 8) in sea stars with mass of 203 g (A), 34 g (B) and 19 g (C). Oscillation frequency of energies decreases with increasing mass (see also Figs 3, 4B). Peaks in ΔE_{kh} and ΔE_p are almost in phase (see also Fig. 7), with the fastest speeds at the highest point in a sea star's stride. Both ΔE_{kh} and ΔE_p increase with increasing size of sea star (see also Fig. 5). The area shaded in grey in B indicates the cycle that is plotted in Fig. 7C. Results shown in C are from Movie 1.

Energies, hodographs and phases

Oscillations in potential and kinetic energy were nearly in phase in the oscillatory gait and the change in potential energy $E_{p,amp}$ was much greater than the change in horizontal kinetic energy $E_{kh,amp}$ (Figs 5, 6, 7, 8b).

During the oscillatory gait, mass of the sea stars accounted for >89% of the variation in the potential and kinetic energy amplitudes with heavier sea stars having higher energy amplitudes (log–log regressions: each $F_{1,52}$>424, each P<0.0001; Fig. 6). The slope was significantly less than 1.3 for both energy amplitudes (each $F_{1,52}$>15, each P<0.001). Variation in potential energy was two orders of magnitude more than variation in kinetic energy (paired t-test on log-transformed data: t_{53}=75, P<0.0001; Figs 5, 6; mean

over all sea stars of $E_{p,amp}/E_{kh,amp}$=185±16; mean±s.e.m.). The mean over all 128 videos of $E_{kh,amp}/E_{k,amp,total}$=0.97±0.002; therefore, $E_{kh,amp}$ represents substantially all of the $E_{k,amp,total}$.

During the oscillatory gait, hodographs for all sea stars were clockwise, with peak vertical velocities preceding peak horizontal speeds by about a quarter of a circle (Fig. 7A). On average, vertical velocities preceded horizontal speeds by 1.58 radians (90.3 deg), which is not significantly different from 90 deg (t-test: P=0.82) (Fig. 8A).

Oscillations in potential and kinetic energy were nearly in phase, with the potential energy peak preceding the kinetic energy peak by
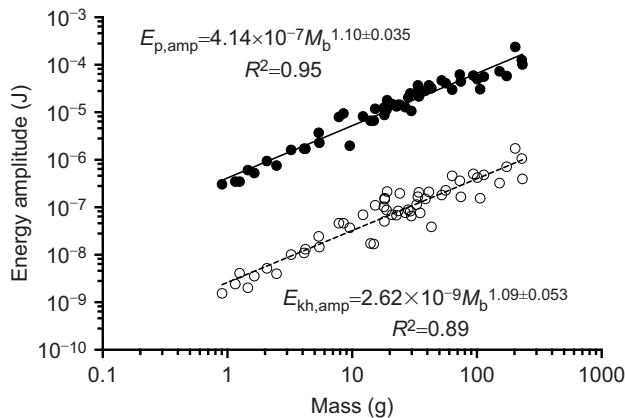
Fig. 6. Logarithmic plot of mean amplitude of potential energy and kinetic energy change during the oscillatory gait as a function of mass. $E_{p,amp}$ (solid line and black circles) and $E_{kh,amp}$ (dashed line and open circles). Errors shown are s.e.m. Filtering with the low pass 1 Hz filter in Mathematica instead of the 30 point moving average used for Fig. 6 slightly increases the coefficients and decreases the exponents (see supplementary Materials and Methods section 4 for further details).

a mean of 0.16±0.15 radians (9.6±8.7 deg; means±s.d.), which is slightly, but significantly, greater than 0 deg (sign test: $P<0.001$; Figs 5, 7B, 8B). This is also significantly different than the slight 1.2 deg phase shift in v_x between the side and bottom cameras (Mann–Whitney U-test, $P<0.001$).

Gravitational versus accelerative forces

Here, we assess the magnitude of forces required to support the underwater weight of the sea stars and compare them to the magnitude of the forces accelerating the sea star in the horizontal and vertical directions. The mean of the ratios of accelerative to gravitational forces for the 54 sea stars used in the kinematic analyses are: $Fr_z=1.8\times10^{-3}\pm1.1\times10^{-4}$ and $Fr_{xy}=3.3\times10^{-3}\pm1.8\times10^{-4}$ (means±s.e.m.), indicating that the vertically-directed forces required to support the sea star are large compared with either the vertical or horizontal accelerative forces (see Table S1 for a comparison of results using low pass filtered data with 1,2,3 and 4 Hz cut offs).

DISCUSSION
Speed and gait

In a general invertebrate textbook, sea star locomotion is described as crawling and smooth, a result of the high number of podia each in a different phase of the power stroke (Brusca and Brusca, 2003); *Pisaster giganteus* in particular is described as crawling but we have seen this species using the vertically oscillating gait. Although also describing sea star locomotion as a crawl, Cole (1913) nevertheless observed that the motion was not a smooth glide but proceeded in short lunges of the body. This description concurred with Jennings (1907), who described it as a 'crawl' and 'creep' but also gave detailed observations of 'steps', comparing the motion to the steps of higher animals, and describing a slight elevation of the body, as the body swung over the podia. Only one paper (Montgomery and Palmer, 2012) provides direct data showing that *Patiria miniata* increases gradually in speed until a plateau in speed is reached – a plateau in which there is oscillating vertical motion and oscillating forward speed. Despite observing what we can recognize in hindsight as a gait transition, this transition is not specifically recognized as such in that paper. One characteristic of a gait is that it

operates over a specific range of speeds. The focus of most recent literature on sea star locomotion has been on speeds in various ecological contexts. Although these contexts are sometimes classified as 'pursuit' or 'escape', these speeds are given without regard to gait. A recognition and description of gait requires a description of several elements that define a gait such as speed ranges in which a gait is used and the characteristic patterns of motion or kinematics of the gait.

Fundamental to the definition of gait, is that characteristic kinematic quantities change discontinuously as speed changes (Alexander, 1989). What we observed is a change in the pattern of motion as speed increases (Figs 2, 3B,C and 7A,B). As the speed increases, at some point vertical oscillations are established and phase relationships develop between vertical and horizontal speed oscillations. Specifically, in Fig. 7A,B the colorful squiggles represent 25 s during which the sea star is crawling and the velocity is increasing. Subsequently, during the period when vertical oscillations occur, the hodograph is a series of clockwise circles.

Gaits are typically used over a range of speeds. For instance, walk, trot and gallop are gaits that can each be used over a characteristic range of speeds in horses, although there is an energetically optimal gait within specific speed ranges (Hoyt and Taylor, 1981). Similarly, humans can walk at a variety of speeds with a variety of stride lengths and frequencies, but there is a combination of stride length and frequency that feels more natural and may be more efficient (Kuo, 2001, 2007; Kuo et al., 2005). We have no information about the energetic consequences of the crawling versus oscillatory gait for sea stars, however, the crawling gait seems to be used over a wide range of speeds; after the transition to the oscillatory gait the highest speeds are attained and variation in speed is less (Fig. 3).

What causes this change in gait? One idea is that the faster, oscillatory gait may be a necessary consequence of podial dynamics. Heydari et al. (2020) developed a model of podial actions that described an emergent patterning in the coordination of the podia that was associated with the bouncy gait. We have observed that podial action during the crawl is not obviously coordinated but that it transitions to an oscillatory gait in which there is an alternation between coordinated elongated podia at the highest point in each step followed by the much shorter or collapsed podia at the bottom of each step (see Fig. 7D,E).

How does theory inform frequency predictions?

The hallmark of the bouncy gait is the rhythmic vertical oscillation of the sea star accompanied by cyclical horizontal and vertical velocity changes. We have observed that the frequency of these oscillations is regular and specific to a sea star. That is, sequential cycles in the same sea star have similar periods, a given sea star tends to oscillate at a certain frequency, and frequency decreases with sea star mass (Figs 3, 4B, 5). In the sections below, we develop a simple abstract model and ask: what calculation predicts the observed frequencies? The goal is to develop a conceptual understanding that allows us to predict the observed frequencies and abstracts what is happening in the steps.

Model description

Consider a pendulum bob with a mass M_{PB} at the end of a massless rod of length l with the rod rotating about a pivot point at the end of the rod opposite to the mass (Fig. 9). The rod is caused to oscillate by a moment generated by the vertical force driving the motion and the rod's position is described by the angle θ to the vertical. That vertical force F_z is the sum of forces due to podial pressure F_{z_p} that opposes the sum of gravitational and bouyant forces $F_{z_{gb}}$ (Eqn 3).
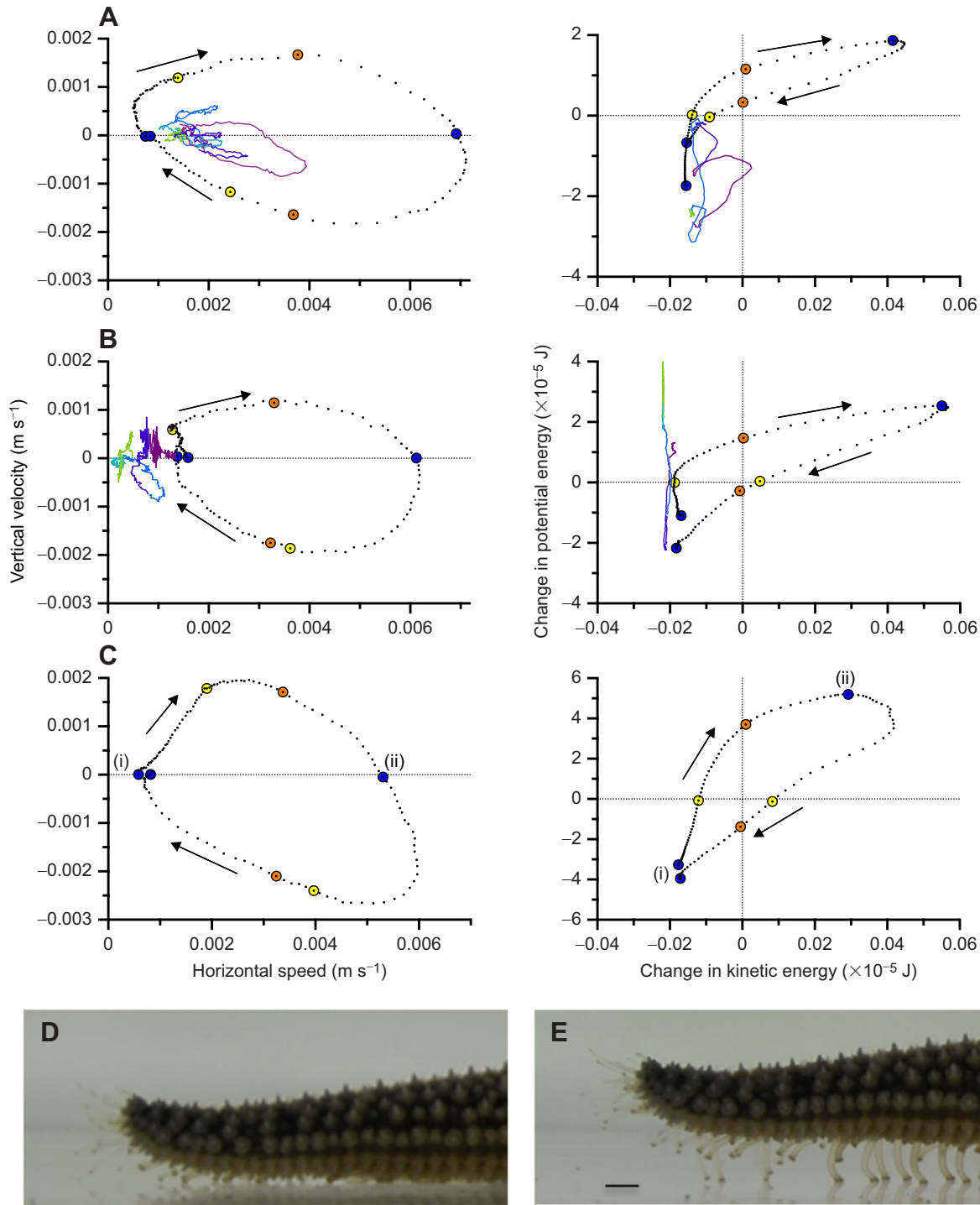
Fig. 7. One oscillatory step for three sea stars. (A) A 24 g sea star, data plotted indicated by grey area in Fig. 2. (B) A 41 g sea star, data plotted indicated by grey area in Fig. 3B. (C) A 34 g sea star, data plotted indicated by grey area in Fig. 5B. The steps are shown as hodographs (left): a parametric plot of v_z and v_{xy} over the time of one step, and a parametric plot of ΔE_p and ΔE_{kh} over the time of one step (right). All data shown are one second moving averages with points 1/30 s apart. Arrows indicate direction of time. The oscillations shown took 3.7 (A), 4.1 (B) and 4.4 s (C). Dotted vertical and horizontal lines indicate mean values for the corresponding variables for the corresponding cycle. Blue points (i) and (ii) in C correspond to the lowest and highest position of the sea star as indicated by the leading arm of the sea star as shown in images D and E, respectively. Yellow and orange points in A–C correspond to identical points in left and right graphs, which occur at the mean change in potential energy and kinetic energy, respectively. Colored lines in A and B plot the first 25 s of crawling data from the figures indicated above in 5 s intervals (green to purple). Contrast the hodograph pattern of the early crawling period to the clockwise ovals during the oscillatory gait. Scale bar: 3 mm.

For simplicity, we consider that F_{z_p} and $F_{z_{gb}}$ act at the same point. Using mass M_b for the inertial term and mass minus fluid displaced ΔM_b in the F_z term and using the small angle approximation that $\sin\theta \approx \theta$, the moments about the pivot point are:

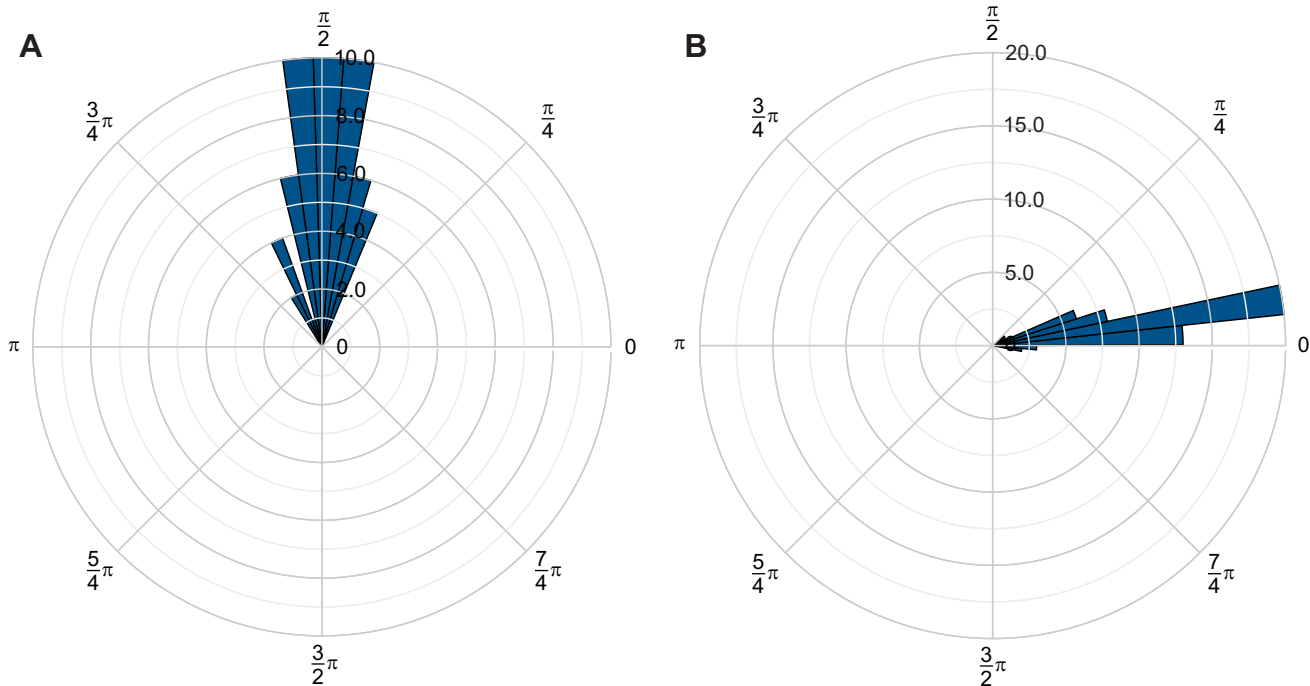$$F_z\, l\, \theta(t) = -M_b\, l^2\, \theta''(t), \tag{23}$$

Fig. 8. Polar histograms for the velocity and energy phase differences of all sea stars. (A) Phase differences between v_z and v_{xy}. (B) Phase differences between E_p and E_{kh}. Data in each histogram are the angular means of all the videos of each individual sea star. For (A) v_z preceded v_{xy} and for (B) E_p preceded E_{kh} by the phase shift shown.

where

$$F_z = F_{z_p} - F_{z_{gb}} = P\,A - \Delta M_b \boldsymbol{g}, \qquad (24)$$

where P is podial pressure and A is the horizontal plane cross-sectional area of all of the actively lifting podia.

Eqn 23 is mathematically equivalent to placing a spring at the fulcrum that exerts a torque that counteracts the $F_{z_{gb}}$ torque. Using a torque spring in a walking model is not unprecedented. Biswas et al. (2018) found that both an inverted pendulum and a SLIP model cannot model observed features of walking at low Froude numbers (<0.1) and instead incorporated an angular spring to model low Froude number walking in fruit flies. An angular spring has also been incorporated in a version of the standard SLIP model used to analyze the human walking gait (Antoniak et al., 2019). Mathematically, the angular spring has the effect of creating a stable inverted pendulum without a feedback control if the moment from the spring is larger than the moment from gravity. This condition is met if $PA > \Delta M_b\,\boldsymbol{g}$. In that case, Eqn 24 is equivalent to a force acting on the bob of the pendulum directed upwards and opposing $F_{z_{gb}}$. The system then acts as if there was a net force field acting upwards causing the inverted pendulum to swing in a manner analogous to an ordinary pendulum in a gravitational field.

This approximation is suitable for application to sea star locomotion because the observed accelerations and accelerative forces are small compared to the gravitational force (Fr_{xy} and Fr_z <10^{-2}). Since the podia are causing all forces other than $F_{z_{gb}}$, then the fact that the accelerative forces are relatively small implies that the podial forces F_{z_p} are aligned with gravity and slightly larger than $F_{z_{gb}}$. This pattern of forces mimics the assumed forces in our model.

We can solve for angular frequency ω by rewriting Eqn 23 as:

$$\omega^2 \theta(t) = -\theta''(t). \qquad (25)$$

Solutions of Eqn 25 give periodic functions with frequency ω, where:

$$\omega = \sqrt{\frac{P\,A - \Delta M_b \boldsymbol{g}}{l M_b}}. \qquad (26)$$

There are a few unrealistic aspects to this model, which we call a torque stabilized inverted pendulum model (TS-IP). For example, real sea star podia bend and extend, whereas the podia in the model do neither. Also, real upward podial forces vary cyclically during a step, whereas upward podial forces are constant in the model, at least over one step. More involved models in the future, may incorporate those features; the simplified model nevertheless provides insights as will be shown in the following sections.

Consideration of the magnitudes of frequencies observed
In this section, we compare two hypotheses that make different predictions about the frequency of the sea star oscillatory step. The first hypothesis is that fall velocity sets the frequency and the alternative hypothesis is that frequency may be set by the podial forces, PA in Eqn 26, slowing the sea star's descent.

In terms of fall velocity, a person watching the oscillatory gait of a sea star might hypothesize that each underwater step consists of lifting the sea star to its highest point, followed by a free fall to the end of the step, and that falling time might set the frequency of the step. If we assume that the rising and falling halves of the step are approximately symmetrical, then the step time is twice the fall time from height l, which is:

$$\tau_1 = 2\sqrt{\frac{2\,l\,M_b}{\Delta M_b \boldsymbol{g}}}. \qquad (27)$$

Using $\Delta M_b/M_b = 0.11$ from Eqn 21 and using a maximum estimate of l as maximum $2\sqrt{2}\,\mathrm{rms}(\Delta z) = 0.0035$ m, we get $\tau_1 = 0.16$ s,
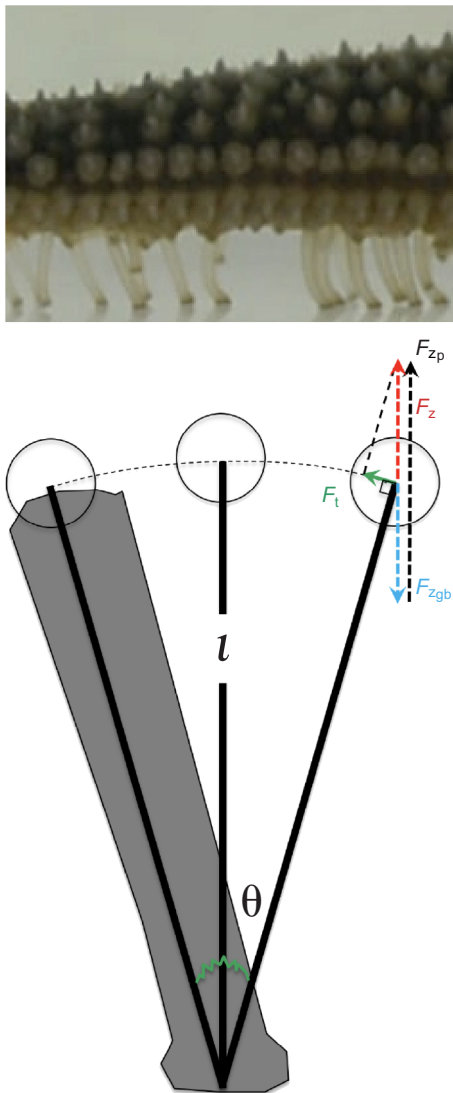
Fig. 9. A sea urchin podium imagined as an inverted pendulum swinging a bob over the podium during a step, where the bob represents the sea star mass. Forces exerted on the bob are gravity minus buoyancy $F_{z_{gb}}$ and the upward force due to podial pressure F_{z_p}. The resultant vertical force F_z has a component, F_t in the direction tangent to the arc of the pendulum. If the forces due to pressure are larger than the forces due to gravity minus buoyancy, then a stable inverted pendulum results and a simple differential equation represents this oscillation as in Eqns 23 and 26 and can be used to predict kinematic patterns and scaling. This is our TS-IP model. The green angle represents the torque spring, which is a conceptual representation of the effect of the tangential forces exerted by the vertical forces shown. This model ignores podial length changes and podial bending, which are beyond the scope of the present manuscript.

which is an order of magnitude less than the periods we observed (Fig. 4B, range: 2.5–7.2 s).

We get a similar result if the equation is further adjusted to give the period of a pendulum underwater τ_u (Neill et al., 2007):

$$\tau_2 = \sqrt{\frac{\rho_{PB} + \kappa \rho_f}{\rho_{PB} - \rho_f}} 2\pi \sqrt{\frac{1}{g}}, \qquad (28)$$

where ρ_{PB} is the density of the pendulum bob, ρ_f is the density of the fluid, and κ is the coefficient of added mass. A further adjustment can be made for drag forces, but that adjustment is negligible for low

speeds and will not be considered here. Note, however, that there may be significant damping by tissues and that such damping would have the effect of lowering and broadening the resonance peak of a damped harmonic oscillator.

Using $\rho_{PB}=\rho=1150$ kg m^{-3} (a middle value for the density of a sea star from Fig. 4A), $\rho_f=1025$ kg m^{-3}, and $\kappa=3$ (an upper value from Daniel, 1984), then $\tau_2=0.69$ s. Although similar to our result from Eqn 27, this value is still an order of magnitude less than the observed periods. We can conclude that the periods predicted by fall time and the underwater pendulum are too short and that some other process must be driving the periodicity.

Consider the alternative hypothesis that podial forces control gait frequency. For comparison to Eqns 27 and 28, the corresponding prediction from Eqn 26 is:

$$\tau_3 = 2\pi \sqrt{\frac{l M_b}{PA - \Delta M_b \, g}}, \qquad (29)$$

To the degree that PA is larger than $\Delta M_b \, g$, the step period will be longer than the predictions of Eqns 27 and 28, where the smaller the difference, the longer the step period. For example, if PA is 1% larger than $\Delta M_b \, g$, then the prediction from Eqn 29, with $l=0.0035$ m and $\Delta M_b/M_b=0.11$ is $\tau_3=3.5$ s, which is within the range of periods observed.

We have no direct measurement of the total podial forces, but the observed accelerations provide a parity check for the relative size of PA and $\Delta M_b \, g$. We can estimate the magnitude of PA using the observed accelerations of the sea stars during a step. The vertical upward force of podia on the sea star is of magnitude:

$$F_{z_p} \approx M_b \, \text{rms}(a_z) + \Delta M_b g. \qquad (30)$$

Substituting Eqn 30 into Eqn 26, expressing angular frequency in terms of frequency and using the mean over all sea stars of the experimentally observed $\bar{a}_z$ as an average vertical acceleration and $2\sqrt{2} \, \text{rms}(\Delta z)$ as an average leg length, we get:

$$f = \frac{\omega}{2\pi} = \frac{1}{2\pi} \sqrt{\frac{\bar{a}_z}{2\sqrt{2} \, \text{rms}(\Delta z)}} = 0.13 \text{ Hz}, \qquad (31)$$

which is a period of 7.7 s. This is of the same order of magnitude as the observed frequencies, supporting the hypothesis that podial forces are increasing the period relative to what would be expected due to free fall.

Scaling of oscillatory frequency

For sea stars, we observed that $f \propto M_b^{-0.14}$. This exponent is remarkably similar to the scaling exponent observed for terrestrial vertebrate legged locomotors (mean=−0.16; range: −0.12 to −0.22; Heglund et al., 1974; Pennycuick, 1975; Alexander et al., 1977; Alexander and Maloiy, 1984; Gatesy and Biewener, 1991; Daley and Birn-Jeffery, 2018). Our exponent is also similar to the exponent (−0.14) observed in ghost crabs moving in air (Whittemore et al., 2015). Multiple theories have been advanced to explain this scaling exponent.

Pennycuick (1992) elaborated on and compared two of these theories that predict different scaling of frequency with mass and we will consider these theories in the context of our TS-IP model and sea star data. The first theory is based on scaling arguments of Hill (1950), which focus on the role of muscle in generating force and moments tending to cause oscillations either of the legs or of the center of mass over the legs. The second theory is based on Alexander and Jayes (1983), which focuses on the role of

gravitational forces in producing pendulum-like motions during legged locomotion. We will show below how hypotheses about gravitational and muscle force scalings predict frequency scaling with mass.

Consider scaling predictions using our TS-IP model for the sea star oscillatory gait (Eqn 26). In geometric similarity, $A \propto l^2$, $M_b \propto l^3$ and $\Delta M_b \propto M_b$, but pressure is independent of size. Pressure is generated by muscle stress in the ampullae, which is governed by Laplace's Law, in which the pressure across the ampullar wall ΔP:

$$\Delta P = \sigma \frac{\Delta R}{R}, \qquad (32)$$

where ΔR is ampullar wall thickness, R is the radius of curvature of the ampulla, and σ is muscle stress, which does not scale with length.

Under the first theory, Hill's muscle hypothesis (Hill, 1950), as formulated by Pennycuick (1992), $\Delta M_b \boldsymbol{g} << PA$, so the gravitational term is negligible and angular frequency is:

$$\omega_1 \approx \sqrt{\frac{PA}{l M_b}} \propto l^{-1} \propto M_b^{-\frac{1}{3}}. \qquad (33)$$

This predicted scaling is much steeper than we observed for the sea star oscillatory gait (Fig. 4B); it is also greater than any of the literature values for terrestrial pedestrian locomotion.

Alternatively, under the second theory, assume as we did for τ_3 (Eqn 29), that PA is 1% larger than $\Delta M_b \boldsymbol{g}$, i.e., that $PA = 1.01 \Delta M_b \boldsymbol{g}$, and substituting into Eqn 26:

$$\omega_2 \approx \sqrt{\frac{0.01 \Delta M_b \boldsymbol{g}}{l M_b}} \propto l^{-\frac{1}{2}} \propto M_b^{-\frac{1}{6}} \approx M_b^{-0.17}. \qquad (34)$$

This is the scaling predicted by Alexander and Jayes (1983). Their prediction is that this scaling is expected for geometrically similar animals locomoting at a constant Froude number, i.e., a constant ratio of inertial to gravitational forces. Our assumption that PA is 1% larger than $\Delta M_b \boldsymbol{g}$ is the equivalent of assuming a constant Froude number since the inertial forces ($PA - \Delta M_b \boldsymbol{g}$) are also a multiple of $\Delta M_b \boldsymbol{g}$ under that assumption.

Our interpretation of Eqn 34 is thus that podial forces are recruited to an extent just sufficient to accelerate the sea star upwards and sideways and that this causes the podial forces to follow the size of the underwater gravitational forces as reflected by $\Delta M_b \boldsymbol{g}$. This circumstance is equivalent to a constant Froude number and similar to the analysis of Alexander and Jayes (1983) for vertebrate locomotion. As also noted in their work, the observed exponent is also close to that predicted for elastic similarity by McMahon (1975, $f \propto M_b^{-0.125}$), so we cannot rule out other possible explanations for this scaling in vertebrates or in sea stars.

Scaling of energy
In the sea star oscillatory gait, we found that the amplitude of both the change in kinetic and potential energy scaled identically with mass (Fig. 6). In the following argument, we derive the expected scaling of kinetic and potential energy for a series of geometrically similar animals using legged locomotion in a given medium.

Speed U is a function of step length λ and step time τ:

$$U = \frac{\lambda}{\tau} \propto \frac{M_b^{\frac{1}{3}}}{M_b^{\frac{1}{6}}} \propto M_b^{\frac{1}{6}}, \qquad (35)$$

with τ being $1/\omega_2$ in Eqn 34. Further, assuming leg length $l \propto \lambda$, then, E_p and E_{kh} are:

$$E_p \propto \Delta M_b \boldsymbol{g} \lambda \propto M_b^1 M_b^{\frac{1}{3}} \propto M_b^{\frac{4}{3}}, \qquad (36)$$

and

$$E_{kh} \propto M_b U^2 \propto M_b^1 M_b^{\left(\frac{1}{6}\right)^2} \propto M_b^{\frac{4}{3}}. \qquad (37)$$

If we assume that the oscillations of kinetic and potential energy are proportional to energies in Eqns 36 and 37, then we expect that the slopes of the log-log plots of the rms energies as a function of mass should be straight lines both with slopes equal to $\frac{4}{3} \approx 1.3$. The experimentally determined slopes, both equal to 1.1, are slightly but significantly less (Fig. 6). This underscaling is probably due to the observed underscaling of podial length with mass (Eqn 22) and mean speed with mass (Fig. 4C).
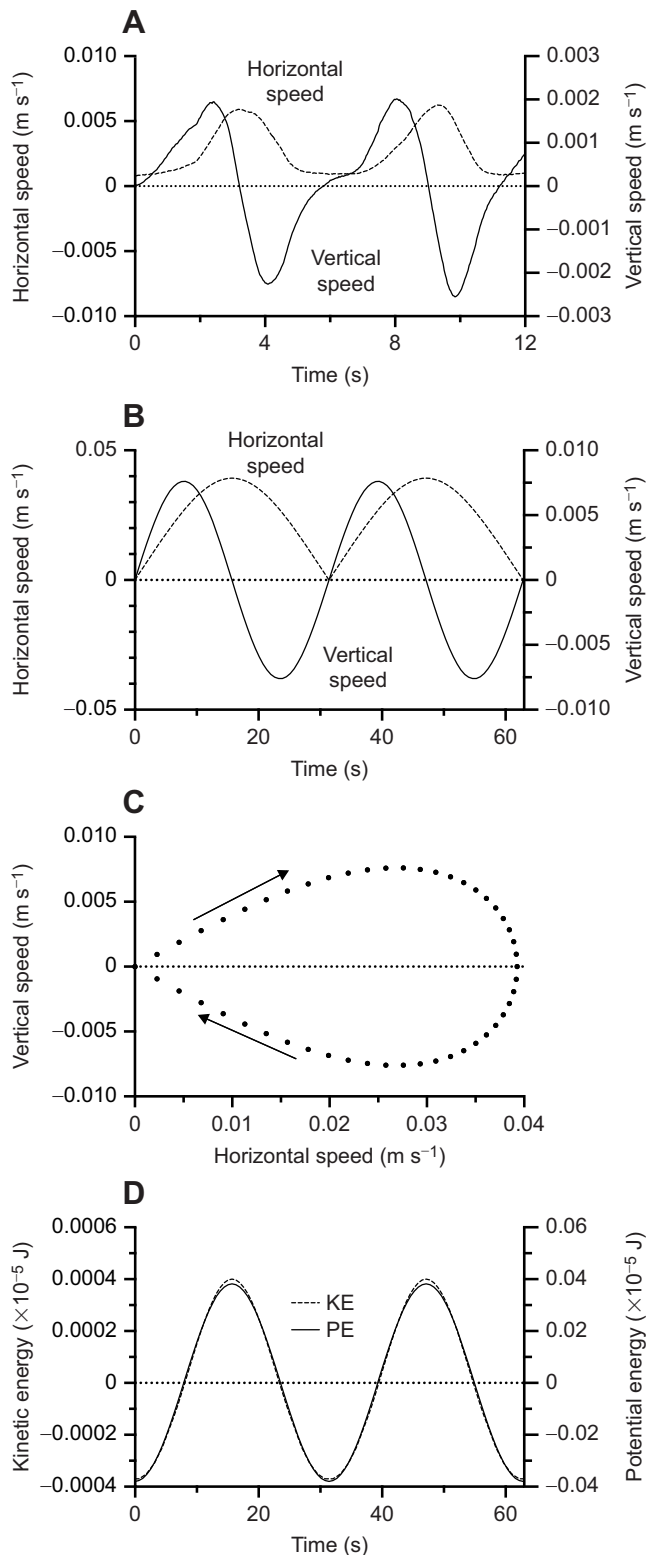
Relationship between potential and kinetic energies and Froude number
Of equal interest to the scaling of energy to mass is the relationship *between* potential and kinetic energy. Two striking features stand out in our analysis: First, $E_{p,amp}$ is two orders of magnitude greater than $E_{kh,amp}$, which precludes the possibility of efficient energy exchange between the two. This is different from the case of terrestrial vertebrate walking where kinetic and potential energy are of similar magnitude and exchange energy. Second, $E_{p,amp}$ precedes $E_{kh,amp}$ by 9.6 deg, and so they are substantially in phase (Figs 5,7,8b), which is a pattern more similar to terrestrial running than walking (Cavagna et al., 1964; Cavagna and Legramandi, 2020), though without an aerial phase. In the sea star bouncy gait, both due to the phase and magnitudes of the kinetic and potential energies, there is clearly no exchange of energies, although because potential energy is larger than kinetic energy, it is likely that some of the potential energy at the top of the bounce is converted to kinetic energy in the second half of each step.

In terrestrial locomotion, considerable attention is paid to the redirection of motion during the ground phase (Kuo et al., 2005; Ruina et al., 2005; Adamczyk and Kuo, 2009). This redirection is associated with energy storage in springs. In the terrestrial running gait the potential and kinetic energies exchange energy with collagen-based springs in the legs that store elastic strain energy (Alexander, 1988; Biewener, 1998; Dickinson et al., 2000). A potential candidate for such energy storage in sea stars could be the collagen fibers that wind around each podium in a cross-fiber helical array and along the long axis of each ampulla (McCurley and Kier, 1995). Our TS-IP model suggests a significant role for podia in slowing the descent of the sea star in the second half of each step, which might provide an opportunity for storage of elastic energy in the podia.

The ratio of kinetic to potential energy occurs in the Froude number. In particular, in an underwater setting, it is appropriate to write an underwater Froude number in the following way:

$$Fr = \frac{M_b U^2}{\Delta M_b \boldsymbol{g} l} = \frac{U^2}{\boldsymbol{g}_e l}, \qquad (38)$$

Fig. 10. Kinematic data predicted by the TS-IP model (Eqn 25). Initial conditions $\theta(0) = -\pi/8$ rad, $\theta'(0)$=0 rad s^{-1} and ω=1 rad s^{-1}. The vertical component is $\cos\theta(t)$ and the horizontal component is $\sin\theta(t)$. (A) Actual pattern for vertical and horizontal speed for two steps of a sea star. The velocity data are from the same video as the energy data shown in Fig. 5A. (B–D) Predictions of patterns and phases; axes units are arbitrary. Compare the predicted pattern in B with data in A, predicted pattern in C with data in Fig. 7 and predicted pattern in D with data in Fig. 5. Note that in D, changes in kinetic energy and potential energy are exactly in phase, whereas in the sea stars changes in potential energy slightly precede changes in kinetic energy (Fig. 8B). For B and C, similar to Figs 7 and 8A, vertical speed precedes horizontal speed by $\pi/2$. Pattern of energies and speeds of the TS-IP model are similar to those observed in the sea star bouncy gait.

numbers, on the order of 10^{-2} to 10^{-3}, than are reported for terrestrial vertebrate locomotors, which are on the order of one, or underwater crabs, which ranged from 0.4 to 3 (Martinez et al., 1998; Chellapurath et al., 2020). For terrestrial vertebrate pedestrians, across a range of species moving naturally, walking Froude numbers have been reported between 10^{-2} and 0.5 (Jayes and Alexander, 1978; Kramer and Sarton-Miller, 2008; Lees et al., 2016; Dececchi et al., 2020), but at those Froude numbers, one expects a walking gait, where potential and kinetic energy are out of phase. In contrast, in the bouncy sea star gait, despite the very low Froude numbers, potential and kinetic energy are in phase. Thus, the bouncy sea star gait represents a novel kinematic pattern. The only other legged locomotion for which similarly low Froude numbers have been reported is the case of slowly stepping fruit flies, where Froude number was between 0.011 and 0.0038 (Biswas et al., 2018). That study concluded that the fruit fly slow walking gait was fit poorly by a standard SLIP model and required an angular spring inverted pendulum model. Thus, studying legged locomotion at extreme Froude numbers expands the range of known legged gaits.

Hodographs and phase relationships for velocities and energies

The parametric plot of horizontal speed on the abscissa and vertical speed on the ordinal axis produces a nearly circular plot that proceeds in a clockwise fashion as in Fig. 7. This implies that the vertical speed function precedes the horizontal speed by a phase shift of about $\pi/2$ (90 deg) as was observed for all sea stars in Fig. 8 and can also be seen in the example in Fig. 2. This phase relationship between the vertical and horizontal speeds is characteristic of the running gait in terrestrial locomotors. Another feature of the sea star bouncy gait is that the fastest horizontal speeds occur when the sea star is highest as can be seen in the example in Fig. 2. This observed pattern of motion is consistent with the pattern of motion described by our proposed TS-IP model. In the following paragraphs we will describe how that pattern of motion arises.

Consider an upright pendulum. At the horizontal ends of travel of the bob, the bob is highest and the speed is zero. In contrast, at the middle of the swing, the horizontal speed is highest and the bob is at its lowest position. Furthermore, the vertical speed is zero at the ends and at the middle of the travel. Thus, for every one angular cycle of the pendulum there is one horizontal cycle of position and velocity and two vertical cycles of position and velocity. This pattern of motion causes the characteristic relationship of kinetic and potential energy in a pendulum with potential energy being highest when kinetic energy is lowest and vice versa. There is an exchange of kinetic and potential energy.

Consider as a contrast the relationships in a stably oscillating TS-IP. As in the case of the upright pendulum, there are twice as many vertical as horizontal cycles of speed and position and the

which is approximately 10× higher in water than in air for a given pedestrian speed and leg length, and assuming animal densities similar to those measured for the sea stars in our study as well as for two species of crabs (Martinez et al., 1998; Chellapurath et al., 2020). We have observed, however, that the kinetic energy is much less than the potential energy in the sea star oscillatory gait, and therefore bouncing sea stars are operating at much lower Froude

number of horizontal cycles equals the number of angular cycles (Fig. 10). The horizontal speed is maximum as the bob passes the center of travel when the vertical position is highest. This causes the kinetic energy and potential energy to be in phase as is the case in running. Thus, the kinetic and potential energy pattern typical of running can be seen as a consequence of inverted pendulum motion over a single foot.

When comparing any pendulum model to a gait, there is a mismatch in that the pendulum goes back and forth, whereas the gait is a series of uni-directional swings over alternating legs. It is possible to mimic this pattern by considering the absolute value of the horizontal location and speeds. In that case the periodicity of the horizontal motion appears to double so that the vertical period is now equal to the horizontal period. In this case the phase shift between the horizontal and vertical speeds is $\pi/2$ as we observed in the sea star bouncy gait.

The patterns of motion shown by our TS-IP model mimic those of the sea star gait. Specifically, the horizontal and vertical speed patterns (Fig. 10A,B) have similar temporal patterns in each cycle, the hodograph (Fig. 10C) is similar to the hodographs in Fig. 8, and the kinetic and potential energies are in phase. The similarity between observed and predicted kinematic patterns shows that, despite its simplifying assumptions, the TS-IP model can replicate some kinematic patterns of the sea star bouncy gait.

Why does speed matter to sea stars?

It seems likely that the high-speed bouncy gait is energetically costly given the synchrony of peaks in kinetic and potential energies. Energy is the currency of evolution and the evolution of a high energy behavior may confer offsetting fitness benefits. Below we speculate on some ways the speed of the bouncy gait may do so.

In general, sea stars are not thought of as high energy creatures. They spend most of their time in sitting in a low energy state, not eating anything. However, sea stars must move to find and capture food and to escape predation. For example, we have observed that the sea star *Luidia clathrata* initiates the oscillatory gait when food is dropped into an aquarium with them. Perhaps these sea stars are competing to reach a prey resource first by moving the fastest. Similarly, *A. forbesi* sped up to 0.002 ± 0.004 m s^{-1} (mean±s.e.m.) when cracked clams were placed in their aquarium (Moore and Lepper, 1997), which is similar to the speeds we observe for this species' oscillatory gait. Speed may not only help sea stars obtain food first, but also to escape becoming someone else's food. For example, faster speeds in the small, surface grazing sea star *Parvulastra exigua* allows it to flee from predation by the larger, slower sea star *Meridiastra calcar*, thereby enabling their co-existence in more resource rich areas of the intertidal (McLaren and Byrne, 2021). Similarly, the sea star *Heliaster helianthus* flees from predation by the sea star *Meyenaster gelatinosus* (Gaymer and Himmelman, 2008). Speed may generally factor into the ability of sea stars to capture not only mobile prey such as other sea stars, but also, for example, to capture other prey such as gastropod snails that escape sea star predation by fleeing (Vermeij, 2020).

References
Adamczyk, P. G. and Kuo, A. D. (2009). Redirection of center-of-mass velocity during the step-to-step transition of human walking. *J. Exp. Biol.* **212**, 2668-2678. doi:10.1242/jeb.027581

Alexander, R. M. (1988). *Elastic Mechanisms in Animal Movement*. Cambridge University Press.

Alexander, R. M. (1989). Optimization and gaits in the locomotion of vertebrates. *Physiol. Rev.* **69**, 1199-1227. doi:10.1152/physrev.1989.69.4.1199

Alexander, R. M. (1995). Simple models of human movement. *Appl Mech Rev* **48**, 461-470. doi:10.1115/1.3005107

Alexander, R. M. (2003). *Principles of Animal Locomotion*. Princeton University Press.

Alexander, R. M. and Jayes, A. (1983). A dynamic similarity hypothesis for the gaits of quadrupedal mammals. *J. Zool.* **201**, 135-152. doi:10.1111/j.1469-7998.1983.tb04266.x

Alexander, R. M. and Maloiy, G. (1984). Stride lengths and stride frequencies of primates. *J. Zool.* **202**, 577-582. doi:10.1111/j.1469-7998.1984.tb05054.x

Alexander, R. M., Langman, V. and Jayes, A. (1977). Fast locomotion of some African ungulates. *J. Zool.* **183**, 291-300. doi:10.1111/j.1469-7998.1977.tb04188.x

Andrada, E., Blickhan, R., Ogihara, N. and Rode, C. (2020). Low leg compliance permits grounded running at speeds where the inverted pendulum model gets airborne. *J. Theor. Biol.* **494**, 110227.

Antoniak, G., Biswas, T., Cortes, N., Sikdar, S., Chun, C. and Bhandawat, V. (2019). Spring-loaded inverted pendulum goes through two contraction-extension cycles during the single-support phase of walking. *Biol. Open* **8**, bio043695.

Arshavskii, Y. I., Kashin, S., Litvinova, N., Orlovskii, G. and Fel'dman, A. (1976). Types of locomotion in ophiurans. *Neurophysiology* **8**, 398-404. doi:10.1007/BF01063602

Astley, H. C. (2012). Getting around when you're round: quantitative analysis of the locomotion of the blunt-spined brittle star, *Ophiocoma echinata*. *J. Exp. Biol.* **215**, 1923-1929. doi:10.1242/jeb.068460

Biewener, A. A. (1998). Muscle-tendon stresses and elastic energy storage during locomotion in the horse. *Comp. Biochem. Physiol. B Biochem. Mol. Biol.* **120**, 73-87. doi:10.1016/S0305-0491(98)00024-8

Bishop, K. L., Pai, A. K. and Schmitt, D. (2008). Whole body mechanics of stealthy walking in cats. *PLoS ONE* **3**, e3808. doi:10.1371/journal.pone.0003808

Biswas, T., Rao, S. and Bhandawat, V. (2018). A simple extension of inverted pendulum template to explain features of slow walking. *J. Theor. Biol.* **457**, 112-123. doi:10.1016/j.jtbi.2018.08.027

Brusca, R. C. and Brusca, G. J. (2003). *Invertebrates*. Sinauer Associates, Inc.

Calisti, M. and Laschi, C. (2017). Morphological and control criteria for self-stable underwater hopping. *Bioinspir. Biomim.* **13**, 016001. doi:10.1088/1748-3190/aa90f6

Cavagna, G. A. and Legramandi, M. A. (2020). The phase shift between potential and kinetic energy in human walking. *J. Exp. Biol.* **223**, jeb232645.

Cavagna, G. A., Saibene, F. P. and Margaria, R. (1964). Mechanical work in running. *J. Appl. Physiol.* **19**, 249-256. doi:10.1152/jappl.1964.19.2.249

Chellapurath, M., Stefanni, S., Fiorito, G., Sabatini, A. M., Laschi, C. and Calisti, M. (2020). Locomotory behaviour of the intertidal marble crab (*Pachygrapsus marmoratus*) supports the underwater spring-loaded inverted pendulum as a fundamental model for punting in animals. *Bioinspir. Biomim.* **15**, 055004. doi:10.1088/1748-3190/ab968c

Cole, L. J. (1913). Direction of locomotion of the starfish (*Asterias forbesi*). *J. Exp. Zool.* **14**, 1-32. doi:10.1002/jez.1400140102

Coughlin, B. L. and Fish, F. E. (2009). Hippopotamus underwater locomotion: Reduced-gravity movements for a massive mammal. *J. Mammal.* **90**, 675-679. doi:10.1644/08-MAMM-A-279R.1

Daniel, T. L. (1984). Unsteady aspects of aquatic locomotion. *Amer. Zool.* **24**, 121–134.

Daley, M. A. and Birn-Jeffery, A. (2018). Scaling of avian bipedal locomotion reveals independent effects of body mass and leg posture on gait. *J. Exp. Biol.* **221**, jeb152538. doi:10.1242/jeb.152538

Dececchi, T. A., Mloszewska, A. M., Holtz, Jr, T. R., Habib, M. B. and Larsson, H. C. (2020). The fast and the frugal: Divergent locomotory strategies drive limb lengthening in theropod dinosaurs. *PLoS ONE* **15**, e0223698. doi:10.1371/journal.pone.0223698

Dickinson, M. H., Farley, C. T., Full, R. J., Koehl, M., Kram, R. and Lehman, S. (2000). How animals move: an integrative view. *Science* **288**, 100-106. doi:10.1126/science.288.5463.100

Ellers, O., Johnson, A., Guttenplan, K. and Motokawa, T. (2014). The bounce in a seastar's step: Classifying gaits in underwater legged locomotion. *Integr. Comp. Biol.* **54**, E59.

Ellers, O., Johnson, A. and Motokawa, T. (2018). Do general theories of locomotion apply to underwater walkers? *Integr. Comp. Biol.* **58**, E57.

Ellers, O., Khoriaty, M. and Johnson, A. S. (2021). Kinematics of sea star legged locomotion. *Dryad Dataset*. doi:10.5061/dryad.2547d7wrq

Farlow, J. O., Robinson, N. J., Turner, M. L., Black, J. and Gatesy, S. M. (2018). Footfall pattern of a bottom-walking crocodile (*Crocodylus acutus*). *Palaios* **33**, 406-413. doi:10.2110/palo.2018.037

Gatesy, S. and Biewener, A. (1991). Bipedal locomotion: effects of speed, size and limb posture in birds and humans. *J. Zool.* **224**, 127-147.

Gaymer, C. F. and Himmelman, J. H. (2008). A keystone predatory sea star in the intertidal zone is controlled by a higher-order predatory sea star in the subtidal zone. *Mar. Ecol. Prog. Ser.* **370**, 143-153. doi:10.3354/meps07663

Griffin, T. M. and Kram, R. (2000). Penguin waddling is not wasteful. *Nature* **408**, 929. doi:10.1038/35050167

Heglund, N. C., Taylor, C. R. and McMahon, T. A. (1974). Scaling stride frequency and gait to animal size: mice to horses. *Science* **186**, 1112-1113. doi:10.1126/science.186.4169.1112

Heydari, S., Johnson, A., Ellers, O., McHenry, M. J. and Kanso, E. (2020). Sea star inspired crawling and bouncing. *J. R. Soc. Interface* **17**, 20190700. doi:10.1098/rsif.2019.0700

Hill, A. V. (1950). The dimensions of animals and their muscular dynamics. *Sci. Prog.* **38**, 209-230.

Hoyt, D. F. and Taylor, C. R. (1981). Gait and the energetics of locomotion in horses. *Nature* **292**, 239-240. doi:10.1038/292239a0

Huffard, C. L., Boneka, F. and Full, R. J. (2005). Underwater bipedal locomotion by octopuses in disguise. *Science* **307**, 1927. doi:10.1126/science.1109616

Jayes, A. and Alexander, R. M. (1978). Mechanics of locomotion of dogs (*Canis familiaris*) and sheep (*Ovis aries*). *J. Zool.* **185**, 289-308. doi:10.1111/j.1469-7998.1978.tb03334.x

Jennings, H. S. (1907). Behavior of the starfish *Asterias forreri* de loriol. *Univ. Calif. Publ. Zool.* **4**, 53-185.

Johnson, A., Ellers, O., Etzel, R. and Khoriaty, J. (2019). The oscillatory gait of high-speed sea stars: Do sea stars of varying morphology vary stride length or step frequency to change speed? *Integr. Comp. Biol.* **59**, E114.

Kramer, P. A. and Sarton-Miller, I. (2008). The energetics of human walking: is Froude number (Fr) useful for metabolic comparisons? *Gait Posture* **27**, 209-215. doi:10.1016/j.gaitpost.2007.03.009

Kuo, A. D. (2001). A simple model of bipedal walking predicts the preferred speed-step length relationship. *J. Biomech. Eng.* **123**, 264-269. doi:10.1115/1.1372322

Kuo, A. D. (2007). The six determinants of gait and the inverted pendulum analogy: a dynamic walking perspective. *Hum. Mov. Sci.* **26**, 617-656. doi:10.1016/j.humov.2007.04.003

Kuo, A. D., Donelan, J. M. and Ruina, A. (2005). Energetic consequences of walking like an inverted pendulum: Step-to-step transitions. *Exerc. Sport Sci. Rev.* **33**, 88-97. doi:10.1097/00003677-200504000-00006

Lees, J., Gardiner, J., Usherwood, J. and Nudds, R. (2016). Locomotor preferences in terrestrial vertebrates: an online crowdsourcing approach to data collection. *Sci. Rep.* **6**, 1-7. doi:10.1038/srep28825

Martinez, M. M., Full, R. and Koehl, M. (1998). Underwater punting by an intertidal crab: a novel gait revealed by the kinematics of pedestrian locomotion in air versus water. *J. Exp. Biol.* **201**, 2609-2623. doi:10.1242/jeb.201.18.2609

McCurley, R. S. and Kier, W. M. (1995). The functional morphology of starfish tube feet: the role of a crossed-fiber helical array in movement. *Biol. Bull.* **188**, 197-209. doi:10.2307/1542085

McLaren, E. J. and Byrne, M. (2021). Predator-prey behavioural interactions between the asterinid seastars *Meridiastra calcar* and *Parvulastra exigua* sympatric on the rocky shores of southeast Australia. *Marine Biology* **168**, 1-11. doi:10.1007/s00227-021-03933-9

McMahon, T. A. (1975). Using body size to understand the structural design of animals: Quadrupedal locomotion. *J. Appl. Physiol.* **39**, 619-627. doi:10.1152/jappl.1975.39.4.619

Minetti, A. and Alexander, R. M. (1997). A theory of metabolic costs for bipedal gaits. *J. Theor. Biol.* **186**, 467-476. doi:10.1006/jtbi.1997.0407

Montgomery, E. (2014). Predicting crawling speed relative to mass in sea stars. *J. Exp. Mar. Biol. Ecol.* **458**, 27-33. doi:10.1016/j.jembe.2014.05.009

Montgomery, E. M. and Palmer, A. R. (2012). Effects of body size and shape on locomotion in the bat star (*Patiria miniata*). *Biol. Bull.* **222**, 222-232. doi:10.1086/BBLv222n3p222

Moore, P. A. and Lepper, D. M. (1997). Role of chemical signals in the orientation behavior of the sea star *Asterias forbesi*. *Biol. Bull.* **192**, 410-417. doi:10.2307/1542750

Nauwelaerts, S., Zarski, L., Aerts, P. and Clayton, H. (2015). Effects of acceleration on gait measures in three horse gaits. *J. Exp. Biol.* **218**, 1453-1460. doi:10.1242/jeb.113225

Neill, D., Livelybrooks, D. and Donnelly, R. J. (2007). A pendulum experiment on added mass and the principle of equivalence. *Am. J. Phys.* **75**, 226-229. doi:10.1119/1.2360993

Pennycuick, C. (1975). On the running of the gnu (*Connochaetes taurinus*) and other animals. *J. Exp. Biol.* **63**, 775-799. doi:10.1242/jeb.63.3.775

Pennycuick, C. J. (1992). *Newton Rules Biology*. Oxford University Press.

Ruina, A., Bertram, J. E. and Srinivasan, M. (2005). A collisional model of the energetic cost of support work qualitatively explains leg sequencing in walking and galloping, pseudo-elastic leg behavior in running and the walk-to-run transition. *J. Theor. Biol.* **237**, 170-192. doi:10.1016/j.jtbi.2005.04.004

Saibene, F. and Minetti, A. E. (2003). Biomechanical and physiological aspects of legged locomotion in humans. *Eur. J. Appl. Physiol.* **88**, 297-316. doi:10.1007/s00421-002-0654-9

Sato, K., Watanuki, Y., Takahashi, A., Miller, P. J., Tanaka, H., Kawabe, R., Ponganis, P. J., Handrich, Y., Akamatsu, T., Watanabe, Y. et al. (2007). Stroke frequency, but not swimming speed, is related to body size in free-ranging seabirds, pinnipeds and cetaceans. *Proc. R. Soc. B* **274**, 471-477. doi:10.1098/rspb.2006.0005

Sato, K., Shiomi, K., Watanabe, Y., Watanuki, Y., Takahashi, A., Ponganis, P. J. (2010). Scaling of swim speed and stroke frequency in geometrically similar penguins: they swim optimally to minimize cost of transport. *Proc. R. Soc. B* **277**, 707-714. doi:10.1098/rspb.2009.1515

Snaterse, M., Ton, R., Kuo, A. D. and Donelan, J. M. (2011). Distinct fast and slow processes contribute to the selection of preferred step frequency during human walking. *J. Appl. Physiol.* **110**, 1682-1690. doi:10.1152/japplphysiol.00536.2010

Usherwood, J. R. (2010). Inverted pendular running: a novel gait predicted by computer optimization is found between walk and run in birds. *Biol. Lett.* **6**, 765-768. doi:10.1098/rsbl.2010.0256

Vermeij, G. J. (2020). Getting out of arms' way: Star wars and snails on the seashore. *Biol. Bull.* **239**, 209-217. doi:10.1086/711487

Whittemore, S., Hoglin, B., Green, M. and Medler, S. (2015). Stride frequency in relation to allometric growth in ghost crabs. *J. Zool.* **296**, 286-294. doi:10.1111/jzo.12244

Kinematics of Sea Star Legged Locomotion
Supplementary Materials and Methods

1 Moving Average and its Assignment to a Point in Time

We calculated moving averages using a 30 point window. The method used to assign the moving average to a point in time varies among algorithms implementing moving averages. In our algorithm, we calculated the moving average of the associated times using a 30 point window and assigned that average to the 30 point average of the associated values (see Figs S1, S2A-C). This ensures that there is no time shift of the averaged signal resulting from the moving average process. This produces a series of values and time points where some points are missing from the beginning and end of the series. It is sometimes useful to renumber the time axis so that it starts at zero time. We did such renumbering in a way that plotted values such as position and velocity at synchronous times. Because it takes two points to produce every velocity point, this sometimes involves additional two point averaging for position data.

2 Filter Effects on Amplitude

Filters affect the amplitude of components of a signal typically reducing the amplitude at some frequencies while maintaining amplitude at other frequencies. In our study we are interested in the low frequency oscillations that occur during the bouncy gait and want to filter out higher frequency noise, probably from digitization and image recognition noise. We use a moving average, which is a kind of low pass filter, as well as a Finite Impulse Response low pass filter both implemented in *Mathematica.*

The effects of a 30 point moving average filter and a 0.8 Hz cutoff low pass filter on a small section of raw z-position data from one video is shown in Fig. S1. In a broader view of data from the same video, position data in our study is nearly unaffected, except for removal of noise, both by filtering using 30 point moving averages and using a 0.8 Hz cutoff low pass filter (Fig. S2A-C). Nevertheless, calculating the x direction velocities reveals high frequency noise (Fig. S2D) that is strongly attenuated by filtering the position data before calculating the velocity. The discrete Fourier transform (DFT) of the z position also shows little impact of filtering on the largest frequency component (Fig. S2E). The DFT transforms of the filtered and unfiltered x velocities illustrate that high frequency noise is attenuated while having little effect on frequencies below 0.5 Hz (Fig. S2F). Frequencies below 0.5 Hz are of primary interest because all of the fundamental frequencies shown in manuscript Fig. 4B are below 0.5 Hz.

A filter should remove noise, in this case higher frequency noise, while retaining as much of the original low frequency components as possible. Typically, a filtered signal will tend to under represent the original signal amplitude at a specific frequency. We can illustrate the effect of 30 point moving average and low pass filters by examining the DFT of a hypothetical signal (Fig. S3A). The hypothetical signal we consider has several equal magnitude, discrete, low frequency components below 3 Hz and smaller random noise at all frequencies. We can see from the DFT that lowest frequencies are represented at almost full magnitude, whereas the higher frequencies are strongly attenuated by the filter. We can also see that the low pass filter has more desirable characteristics in that it is a monotonically decreasing filter versus the lobed nature of the moving average. Nevertheless the moving average is easy to implement and provides similar results.

We now consider the effect of moving average and low pass filters on the data in our study. Because the fundamental frequency varies among sea stars, whereas we used the same 30 point moving average or low pass filter for each video, the effect of filtering will vary somewhat among sea stars. This effect can be assessed by calculating the ratio of the magnitude of the fundamental frequency in the DFT of the filtered data compared to magnitude of the fundamental frequency in the DFT of the raw data. A histogram comparing this ratio between 30 point moving average filtered and 0.8 Hz low pass filtered data is in Fig. S3B. The low pass filter represents the highest magnitude slightly better on average than the 30 point moving average (ratio of 0.96 vs 0.93). But the biggest difference between the effect of the filters is that the moving average has a larger variance in the ratio of filtered to original amplitude. This suggests that the low pass filter would be a better choice for a filter than the moving average. Overall, the use of a 30 point moving average made little difference for most of the analyses in our manuscript, therefore, we retained the use of the simpler 30 point moving average for most analyses.

3 Propagation of Noise as a Function of Frequency Through Velocity, Acceleration, and Kinetic Energy Calculations

The position signal that describes the bouncy, periodic nature of the sea star gait is described as the sum of orthogonal sinusoidal functions with each frequency in the sum being a multiple of the smallest frequency Φ. The velocity and acceleration, given by the first and second derivatives of such a function, have of mathematical necessity the higher frequencies represented by larger amplitudes. This mathematical fact has the consequence that noise at higher frequencies will tend to be over-represented in the derivatives. For example:

$$g(t) = a_0 + a_1 \sin(t\Phi) + a_2 \sin(2t\Phi) + a_3 \sin(3t\Phi) + a_4 \sin(4t\Phi), \tag{S1}$$

and

$$g'(t) = a_1 \Phi \cos(t\Phi) + 2a_2 \Phi \cos(2t\Phi) + 3a_3 \Phi \cos(3t\Phi) + 4a_4 \Phi \cos(4t\Phi), \tag{S2}$$

and

$$g''(t) = -a_1 \Phi \sin(t\Phi) - 4a_2 \Phi \sin(2t\Phi) - 9a_3 \Phi \sin(3t\Phi) - 16a_4 \Phi \sin(4t\Phi), \tag{S3}$$

where $g(t)$ is the position function, $g'(t)$ is the velocity function, $g''(t)$ is the acceleration function, a is amplitude, and t is time. This series of differentiated formulas shows that the higher frequencies contribute linearly more to the first derivative, the velocity, and quadratically more to the second derivative, the acceleration. This means that, in cases where the higher frequency position signal contains noise, even when that noise is relatively small, the noise can overwhelm the signal in the derivatives. Low pass filtering can remove the high frequency noise and allow estimates of the lower frequency signal.

To give a sense for how low pass filtering removes noise while retaining most of the signal, we show examples from one video with a cut off of 1 hz (Fig. S4) and a cut off of 4 hz (Fig. S5). In both the panels showing a parameter value versus time and those showing magnitude as a function of frequency, noise obviously increases with the higher derivatives. Furthermore, in the magnitude vs. frequency plots, the noise in the acceleration at higher frequencies is as big or bigger than any of the lower frequency peaks that reflect the mechanical motion of the sea star. The mechanical motion of the sea star can be readily identified as the low frequency fundamental - the highest low peak - and harmonics occurring at multiples of that peak. In the acceleration graph with the shorter frequency axis (0-4) some of the higher harmonics are as large or larger than the fundamental peak. Because the low pass filtering at 1 Hz preserves most of the fundamental peak and, since the harmonic peaks tend to be considerably smaller in the position and velocity graphs, the 1 Hz filtered signal is a good approximation of the mechanical motion of the sea star. But for the evaluation of acceleration, using a 1 Hz low pass filter removes signal as well as noise. Because noise and signal are difficult to distinguish, we use a series of low pass filters at 1,2,3, and 4 Hz to show a range of estimates in this ambiguous circumstance. Since the calculation of Froude number also includes the use of Root Mean Square (RMS) we will present the results of these calculations after that section below.

4 Velocity Squared and Kinetic Energy with Low Pass Filter

We also did a sensitivity analysis for the kinetic energy calculation. The kinetic energy calculation is sensitive in two ways. Firstly, since we aim to produce a graph of kinetic energy scaling as a function of mass and since fundamental frequency is a function of mass and since our filters - both the moving average and low pass filter - have a larger effect on higher frequencies, there is a possibility that the scaling of kinetic energy as a function of mass would be affected by the filtering. Secondly, the squaring of velocity in the kinematic term generates an harmonic at twice the fundamental frequency and, as seen from the acceleration analysis, higher harmonics also tend to be filtered out. The mechanism by which squaring of velocity produces this enhanced harmonic can be seen as follows. The velocity signal has a form similar to:

$$v(t) = 1 + \sin(t), \tag{S4}$$

so that the change in kinetic energy is proportional to:

$$v^2(t) = (1 + \sin(t))^2 = 1 + 2\sin(t) + \sin^2(t). \tag{S5}$$

A double angle formula implies:

$$\sin^2(t) = \frac{1 - \cos(2t)}{2}, \tag{S6}$$

and substituting Eqn S6 into Eqn S5 gives:

$$v^2(t) = \frac{3}{2} + 2\sin(t) - \frac{\cos(2t)}{2}. \tag{S7}$$

Therefore a signal with a frequency of 1 Hz (Eqn S4) acquires an harmonic with frequency of 2 Hz (Eqn S7). To determine the sensitivity of the kinetic energy versus mass regression on filtering effects, we recalculated the regression in manuscript Fig. 6 with a 1 Hz low pass filter. We used a 1 Hz rather than a 4 Hz cut off for the low pass filter because the velocity squared signal typically shows only one smaller significantly sized harmonic and not the proliferation of higher harmonics of similar magnitude seen in the acceleration signal (Figs S4, S5). And since the fundamental frequency is below 0.5 Hz, the harmonic is below 1 Hz. For the example figures, we chose an example with the strongest harmonic signal in our data; most videos have fewer and smaller harmonics.

The regression in Fig. 6 (scaling of the potential and kinetic energy with mass) was recalculated with position data filtered with the *Mathematica* low pass filter with a 1 Hz cut off frequency. As expected, when compared to the analysis shown in Fig. 6, the figure based on low pass filtered data looked nearly identical and the potential energy scaling did not change much: the exponent changed from 1.10 to 1.09 and the magnitude of the coefficient changed from 4.14×10^{-7} to 4.52×10^{-7}. This change is as expected because the low pass filter allows through more signal, raising the overall amount of potential energy. And because frequency is a function of mass and lower masses have higher frequencies and higher frequencies are more attenuated by the filter, then lower masses will be raised more than higher masses, thus slightly decreasing the slope reported on the curve. Similarly, for the kinetic energy: the exponent changed from 1.09 to 1.03 and the magnitude of the coefficient changed from 2.62×10^{-9} to 4.05×10^{-9}. The changes were thus in the same direction but of a larger magnitude than those seen in the potential energy, because for the kinetic energy there is more signal at higher frequencies. Overall, the conclusion is similar: both potential and kinetic energy depend mostly on mass and changes in potential energy are two orders of magnitude higher than changes in kinetic energy.

5   Root Mean Square as a Measure of Signal Size

The position, velocity, and acceleration signals are constituted of a fundamental frequency and harmonics that can be of similar size (Figs. S4, S5). The root mean square (RMS) is a useful way to measure the size of a signal composed of several frequencies of interest.

For a function:

$$f(t) = a + b\sin(t) + c\sin(2t) + d\sin(3t) \tag{S8}$$

the root-mean-square of the function is:

$$RMS(f(t)) = \sqrt{\frac{1}{2\pi - 0} \int_0^{2\pi} f(t)^2 \, dt} = \frac{\sqrt{2a^2 + b^2 + c^2 + d^2}}{\sqrt{2}} \tag{S9}$$

The above relationships (Eqns. S8, S9) are true for orthogonal functions (e.g. sums of different frequencies) and for time periods that are multiples of 2π and are also approximately true for sufficiently long time periods even if not multiples of 2π. Thus the RMS is a way of describing the size of a signal and has a well-defined mathematical relationship to the amplitudes of the constituent signals. The RMS does not underrepresent the amplitude of a signal; it is merely a different expression of the size of a signal. Furthermore it provides a way to measure the size of a signal composed of several frequencies. We used the RMS to provide a summary measure of acceleration size for the purpose of estimating Froude number as described in the manuscript.

6 Sensitivity Analysis of the Effect of Low Pass Filter Cut Off Frequency on Estimates of Froude Number

Froude number was calculated as detailed in the paper and the values given in Table S1 are the means and standard errors for all sea stars for the vertical Froude number and the horizontal Froude number. The real Froude numbers are probably somewhere in the middle of these values since $\Omega = 4$ does include significant noise and $\Omega = 1$ is probably missing some real signal.

Table S1. The effect of the low pass filter cut-off frequency, Ω, on the mean Froude number esti-mates.

Ω	Fr_z	s.e.m.	Fr_{xy}	s.e.m.
1	0.0018	± 0.00011	0.0033	± 0.00018
2	0.0025	± 0.00014	0.0048	± 0.00027
3	0.0032	± 0.00016	0.0060	± 0.00032
4	0.0037	± 0.00017	0.0068	± 0.00036
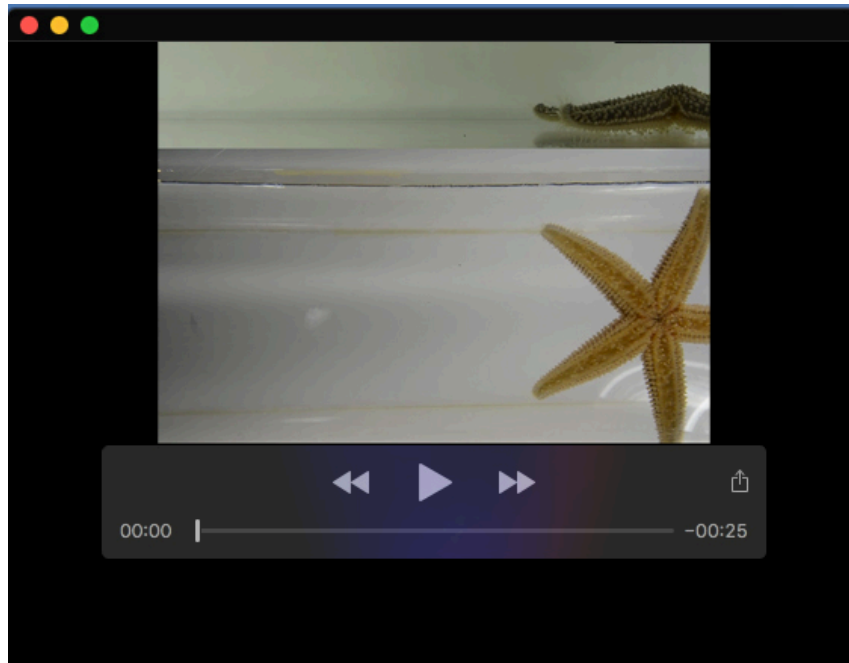
Movie 1. Simultaneous views from the side and bottom cameras showing the sea star whose data is shown in Fig. 5C. This composite video was made from the original side and bottom videos. It was prepared by inserting the original videos into PowerPoint to get composite side and bottom videos, playing them simultaneously in PowerPoint, and taking a QuickTime movie of the composite videos. Frame rate and resolution are likely altered relative to the originals, so these supplemental videos should not be used by readers to obtain data.
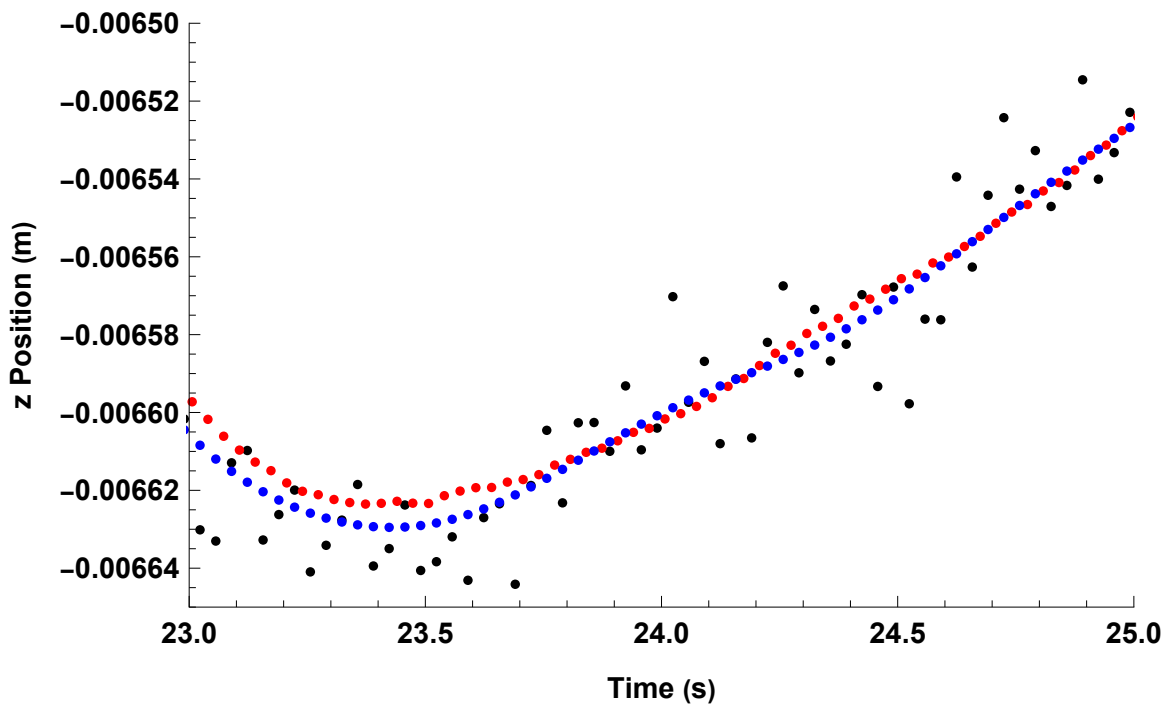
Fig. S1. Close up of z position data, shown in Figure S2C, showing the scatter in the raw data (black), and the effect of a 30 point moving average (red) and a 0.8 Hz low pass filter (dark blue). Note that the black and blue points line up in time and that each red point falls between each pair of black points; those red points have been correctly positioned in time by the 30-point moving average process we describe. There is an optical illusion that sometimes the red points appear closer to one side or the other of the gap.
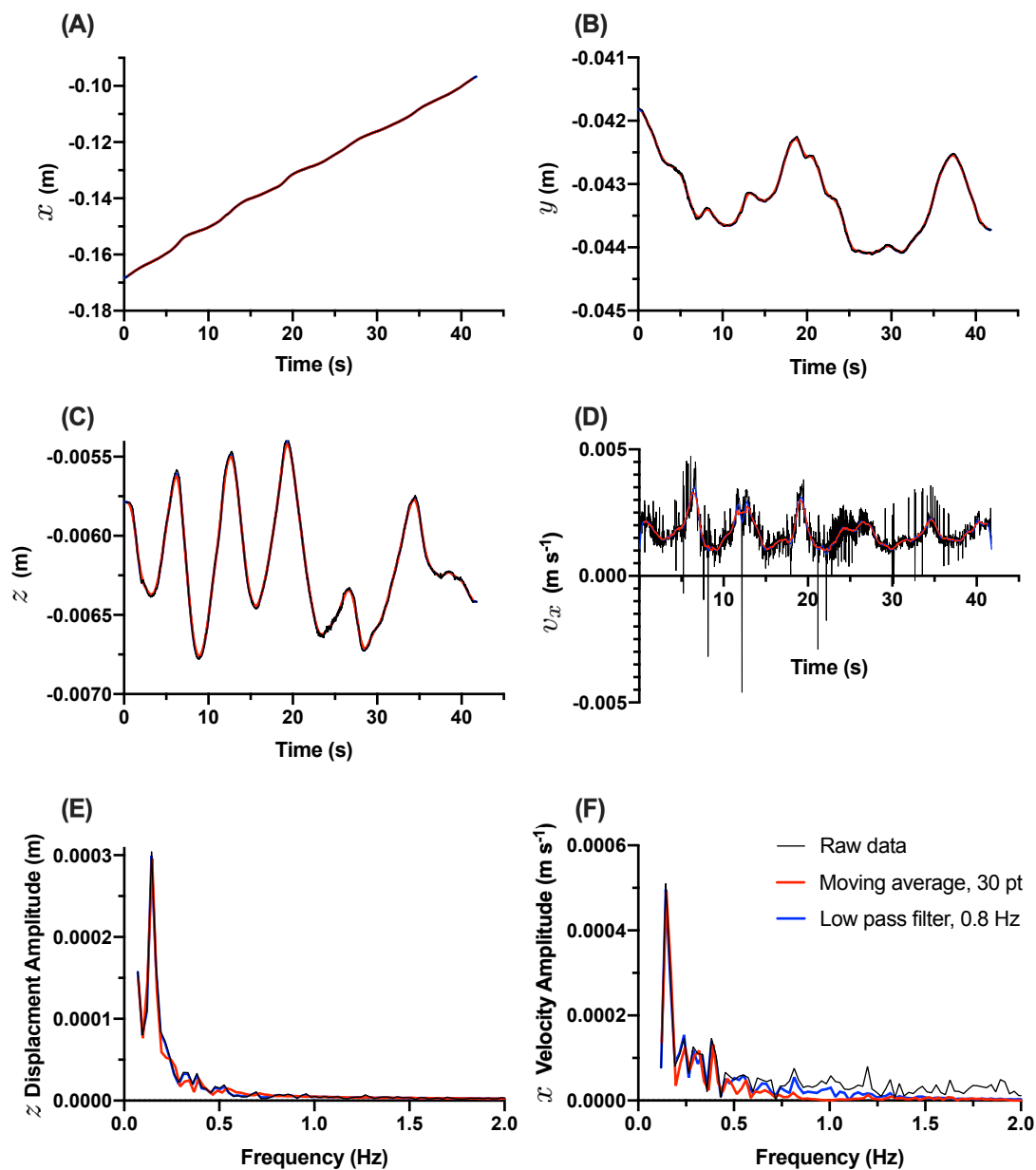
Fig. S2. For one example sea star video, raw data (black), 30-point moving averages (red), and 0.8 Hz low pass filtered (dark blue) position for (A) x, (B) y and (C) z axes as well as (D) x-velocity. Note that the position data appears to be similar filtered and unfiltered but the velocity data reveals high frequency noise. The Fourier transformed (E) z displacement and (F) x velocity show the effect of filtering out the high frequency noise.
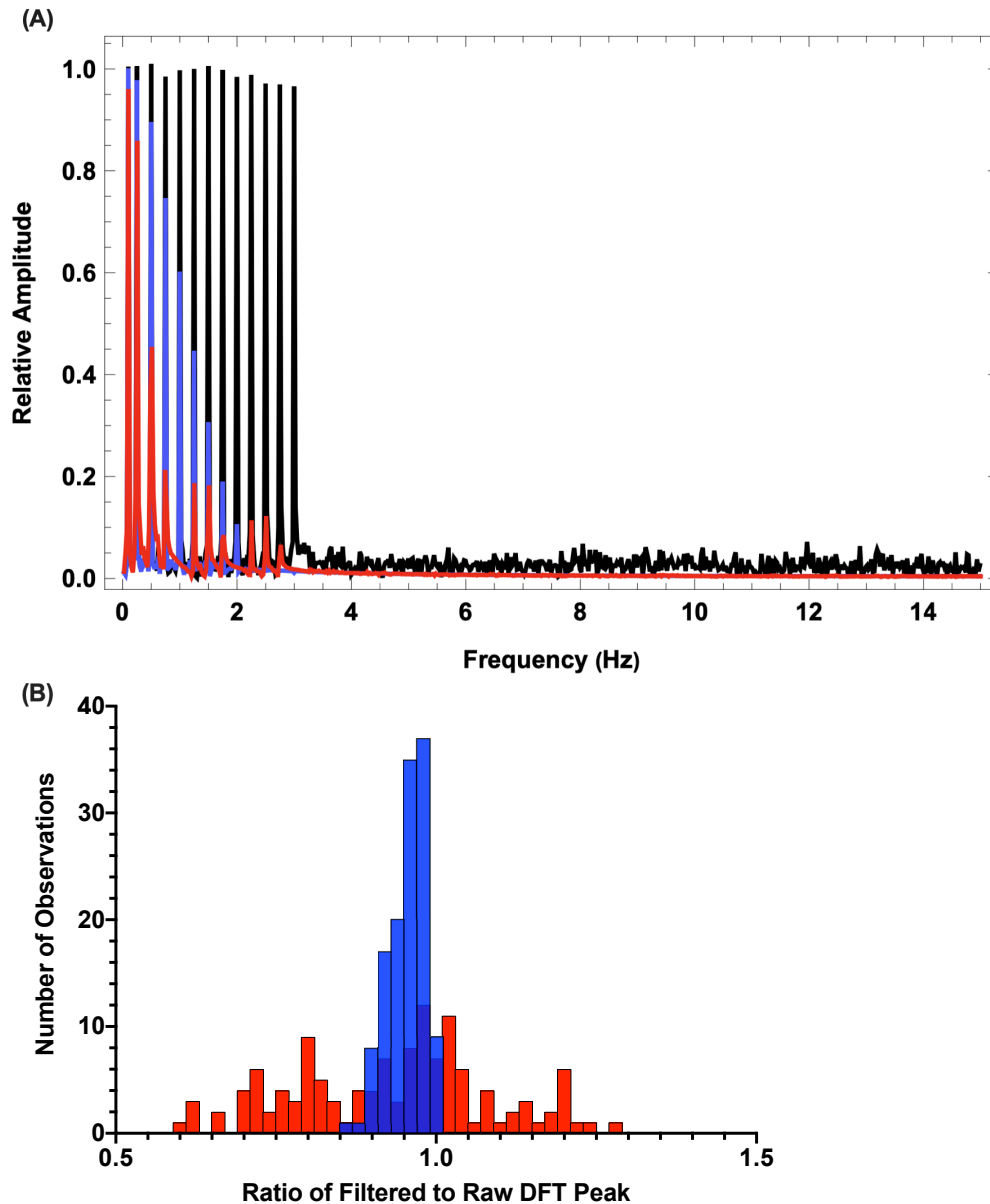
Fig. S3. (A) Discrete Fourier transforms (DFTs) of a hypothetical raw signal sampled at 30 Hz (black), a low pass 1 Hz filtered signal (light blue), and a 30 point moving average filtered signal (red). The hypothetical raw signal has random noise and several discrete frequency signals at intervals below 3 Hz. The low pass filter is implemented in *Mathematica* with a cut-off frequency of 1 Hz. The cut-off frequency is represented at half its raw amplitude. Note that the 30 point moving average filter attenuates the signal more than the 1 Hz low pass filter and that the 30 point moving average filter has a typically lobbed shape with notches at 1 and 2 Hz whereas the low pass filter decreases monotonically. (B) Histogram of the number of sea star videos with each ratio of filtered to raw Fourier transform peak. We calculated the ratios of the maximum amplitude in each Fourier transform of the moving average filtered (red) and 0.8 Hz low pass filtered (dark blue) x-velocity in each video to the maximum peak in the Fourier transform of the raw x-velocity. Means of the ratios are 0.93 ± 0.15 s.d. for the moving average and 0.96 ± 0.028 s.d. for the low pass filter. However, the low pass filter has a much lower variance.
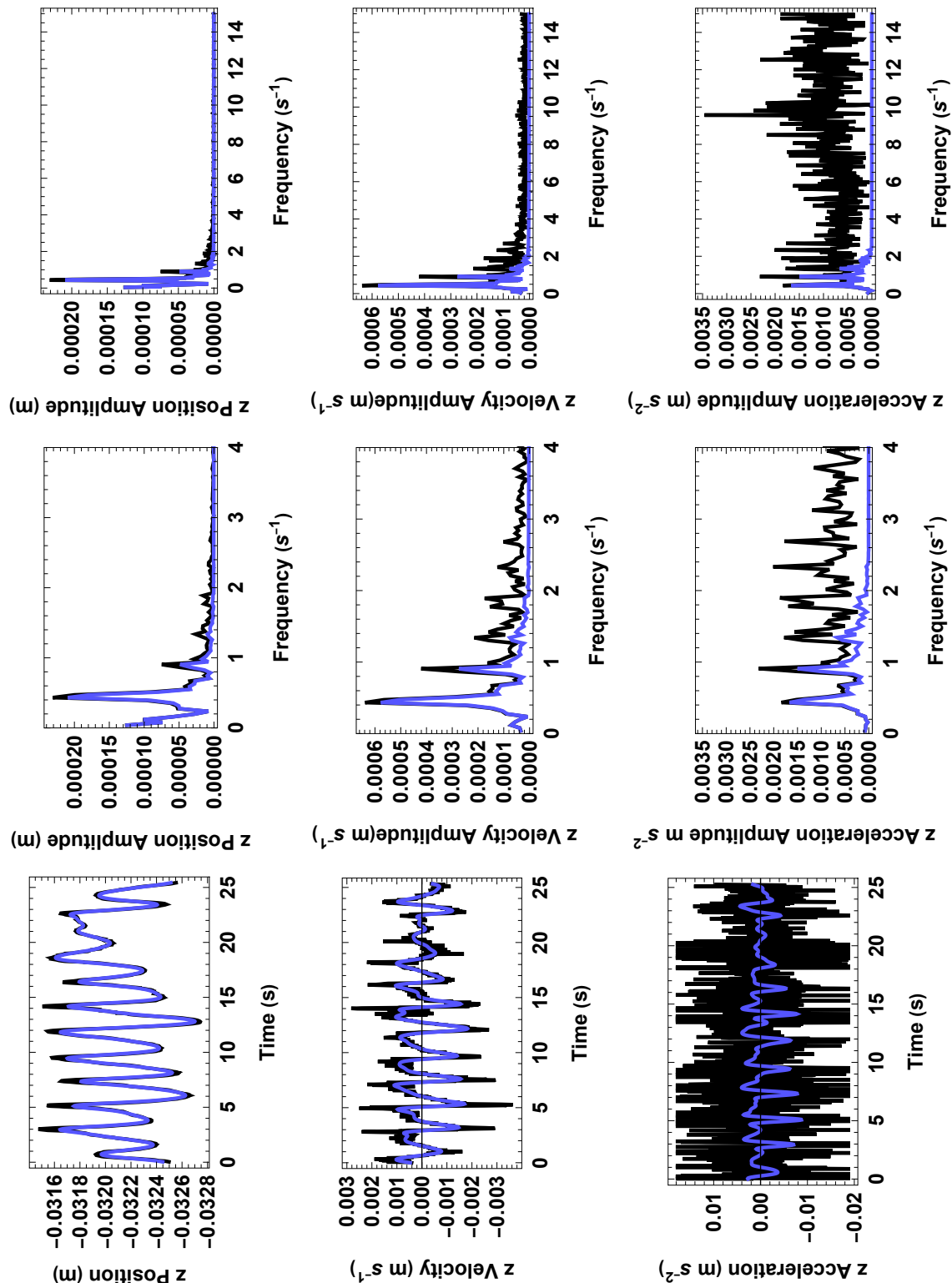
Fig. S4. Example of the raw signal (black lines) filtered using the *Mathematica* low pass filter with a cut-off frequency of 1 Hz (light blue lines). First column is z-position, z-velocity, and z-acceleration data as a function of time; second and third columns are discrete Fourier transforms (DFTs) of those data, with 0-4 Hz displayed in the second column and 0-14 Hz displayed in the third column. The cut-off frequency is represented at half its raw amplitude.
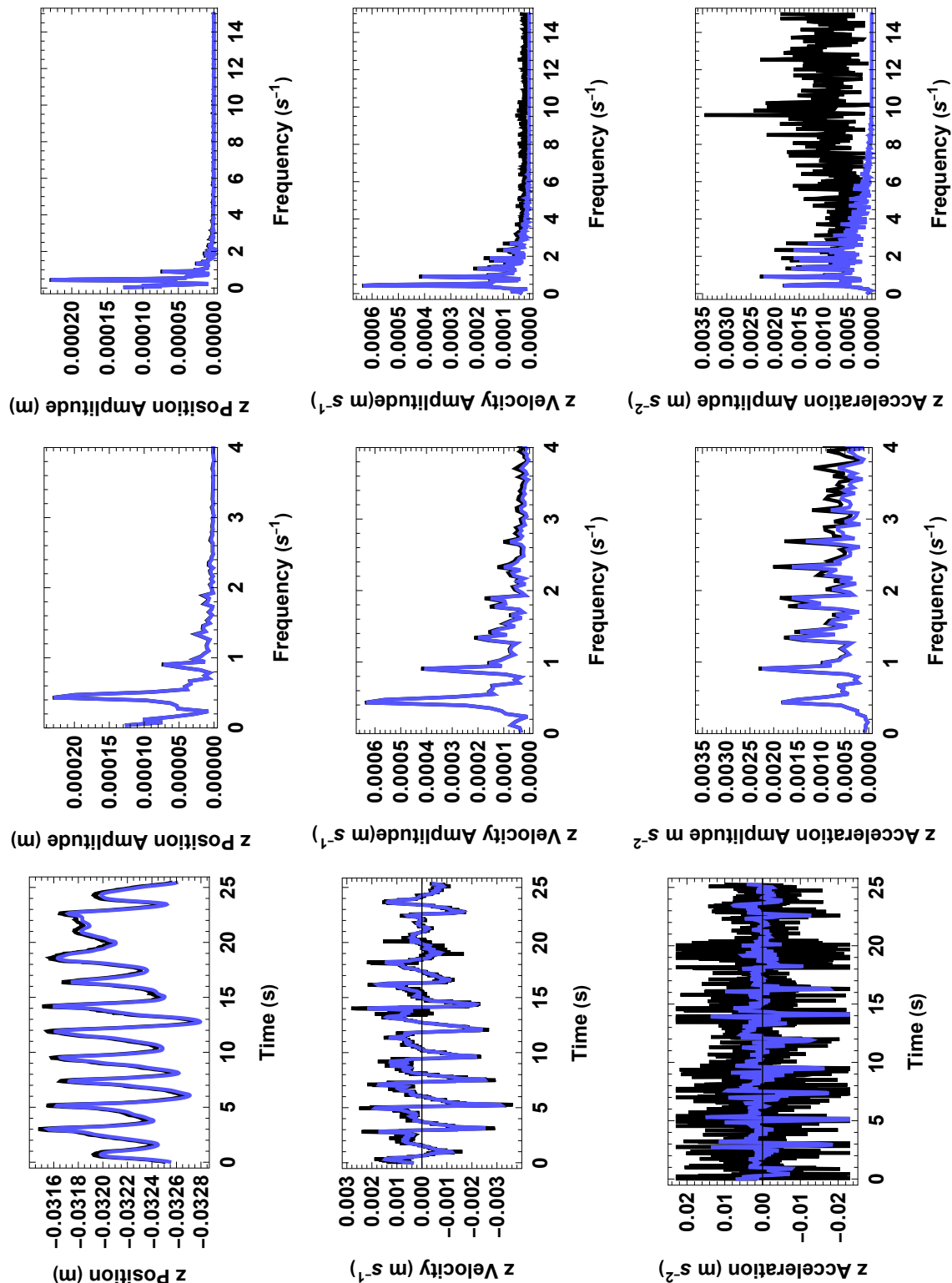
Fig. S5. Example of the raw signal (black lines) filtered using the *Mathematica* low pass filter with a cut-off frequency of 4 Hz (light blue lines). First column is z-position, z-velocity, and z-acceleration data as a function of time; second and third columns are discrete Fourier transforms (DFTs) of those data, with 0-4 Hz displayed in the second column and 0-14 Hz displayed in the third column. The cut-off frequency is represented at half its raw amplitude.